

A Comprehensive Review for MRF and CRF Approaches in Pathology Image Analysis

Chen Li, Yixin Li, Changhao Sun, Hao Chen, Hong Zhang

Abstract—Pathology image analysis is an essential procedure for clinical diagnosis of many diseases. To boost the accuracy and objectivity of detection, nowadays, an increasing number of computer-aided diagnosis (CAD) system is proposed. Among these methods, random field models play an indispensable role in improving the analysis performance. In this review, we present a comprehensive overview of pathology image analysis based on the markov random fields (MRFs) and conditional random fields (CRFs), which are two popular random field models. Firstly, we introduce the background of two random fields and pathology images. Secondly, we summarize the basic mathematical knowledge of MRFs and CRFs from modelling to optimization. Then, a thorough review of the recent research on the MRFs and CRFs of pathology images analysis is presented. Finally, we investigate the popular methodologies in the related works and discuss the method migration among CAD field.

Index Terms—MRF, CRF, Pathology Analysis

I. INTRODUCTION

A. Markov Random Fields

MARKOV *Random Fields* (MRFs) is a type classical undirected *Probabilistic Graphical Model* within the Bayesian framework [1]. Each object in the MRFs is modeled as a random variable, which is called a node (or vertex or point) in a graph, and connected by an edge between them. In image analysis domain, the MRFs can describe the pixel-spatial interaction due to its structure and thus is originally developed to analyze the spatial relationship of physical phenomena. However, the number of possible states of MRFs is excessively large and its joint distribution is hard to be calculated [2].

In 1971, Hammersley and Clifford proved the equivalence between the MRFs and Gibbs distribution and this theory was lately developed by Besag [3]. The joint distribution of MRF is modeled by an explicit and elegant formula due to the MRFs-Gibbs equivalence, where the probability is described by a potential function [4]. The proposed optimization algorithms such as Iterative Condition Mode (ICM) and Expectation Maximization (EM) and MRFs-Gibbs equivalence make the

MRFs a practical model. Additionally, as mentioned above, the MRF model considers the important spatial constraint, which is essential to interpret the visual information. Hence, the MRFs have attracted great attention from scholars since proposed.

The first time that the MRFs applied to solving segmentation problems is in [5], where it is only used for medical image analysis. Through persistent and in-depth research in last two decades, the MRFs are widely used for computer vision problems such as image segmentation, image reconstruction and image classification [6]. However, the MRFs also have limitations: The underlying generative nature of MRFs, which models the joint probability of the images and its corresponding labels, makes it more complicated than needed. The high difficulty of parameter estimation due to the huge amount parameters based on it becomes the bottleneck of its growth [7].

B. Conditional Random Fields

Conditional Random Fields (CRFs), as an important and prevalent type of machine learning method, are designed for building probabilistic models to segment and label sequence data. The CRF is an undirected discriminative graphical model focusing on posterior distribution of observation and possible label sequence as opposed to the generative nature of MRF [8]. The CRFs are developed on the basis of Maximum Entropy Markov Models (MEMMs) in 2002 [9], with the aim at avoiding the fundamental limitations of it and other directed graphical models like Hidden Markov Model (HMM) [10].

Compared to the Bayesian models proposed before, the CRF models have three main advantages: First, the CRF models solve the label bias problem of MEMMs, which is its main deficiency. Second, the CRF models specify the probabilities of label sequence given an observation sequence (condition probability). Compared to other generative models whose parameters are usually trained to maximize the joint likelihood, the CRFs are not necessary to enumerate all possible observation sequences, which is typically intractable. Thirdly, the CRFs relax the strong dependencies assumption in other Bayesian models based on directed graphical models and are capable of building higher-order dependencies, which means that the results of CRFs are more closer to the true distribution of the data. The CRF models have many different variants, such as Fully-connected CRF (FC-CRF) and deep Gaussian CRF. The Maximum A Posteriori Estimation (MAP) algorithm is usually utilized to learn parameters of this model [11].

Chen Li, Yixin Li, Changhao Sun is with Microscopic Image and Medical Image Analysis Group, MBIE College, Northeastern University, China (e-mail: lichen201096@hotmail.com).

Hao Chen was School with Nanjing University of Science and Technology, Nanjing, China.

Hong Zhang was with Shengjing Hospital of China Medical University, China.

The CRFs are attractive in the field of machine learning and approved to achieve good performance in various fields of research, such as for Name Entity Recognition Problem in Natural Language Processing [12], Information Mining [13], Behavior Analysis [14], Image and Computer Vision [15], and Biomedicine [16]. In recent year, with the rapid development of deep learning (DL), the CRF models are usually utilized as an essential pipeline within the deep neural network in order to refine the image segmentation results [7]. Some researches [14] incorporate them into the network architecture, while others [17] include them into the post-processing step. Studies show that they mostly achieve better performances than before.

C. Pathology Analysis

The term pathology has different meanings under different conditions. It usually refers to histopathology and cytopathology, and under other circumstances it refers to other subdiscipline. To avoid confusion, the term pathology refers to histopathology and cytopathology in this paper, which detect morphological changes of lesion like tissue and cellular structure under microscope. In order to obtain a tumor sample, it is necessary to perform a biopsy or aspiration requiring an intervention such as an image-guided procedure or endoscopy [18].

According to World health Organization (WHO), pathology analysis is one of the key elements of early diagnosis of various diseases, especially cancer [19]. Cancer is now responsible for nearly 16.7% death in the world, and over 14 million people are diagnosed as cancer every year. It is found that the ability to provide screening and early cancer diagnosis has a huge impact on improving the curing rate, reducing mortality over cancer and cutting treatment costs, because the main problem now is many cancer cases are diagnosed too late [20]. An accurate pathologic diagnosis is critical, and the reasons are as follows: First, the definitive diagnosis of cancer and other diseases like retinopathy must be made by morphological and phenotypical examination of suspected lesion. Second, especially for cancer, pathology analysis is essential to determine the degree of tumor spread from the original site, which is also called staging. Thirdly, the applicable treatment afterwards relies on various pathologic parameters [18], [21].

Traditionally, pathology results are provided by manual assessment. However, due to the laborious and tedious nature of pathologists work as well as the complexity and heterogeneity of pathology images, the manual analysis is relatively subjective and even leads to misdiagnosis [22]. With the rapid advance of technology, Computer-Aided Diagnosis (CAD) emerges, which promises hopefully more standardized and objective diagnosis comparing to manual inspection. Besides, CAD has the capacity to offer quantitative result. Over the past few decades, there have been extensive researches in CAD area, proposing various algorithms combining prior knowledge and training data in order to assist pathologists in clinical diagnosis and researchers in studying disease mechanisms [23].

D. Motivation

Pathology analysis plays an important role in disease detection. However, manual detection of microscopic images requires exhaustive examination and analysis by a small number of experienced pathologists, and the detection results may be subjective and vary from different pathologists. Especially for Whole-slide Images (WSIs), which are extensively large (e.g., $100,000 \times 200,000$ pixels), it is labor-intensive and time-consuming to achieve fine-grained results [24]. Therefore, various CAD systems are introduced to assist pathologists in detecting diseases. In pathology analysis process, image labeling, serving as the intermediate step, is in a significant position. To some degree, the accuracy of the whole process is highly associated with the quality of the image labeling part. In terms of labeling part, each pixels label is not only related to its individual information, but also depends on its neighborhood [7]. For example, supposing there is a WSI divided into patches, when a patch is labeled as tumor, the probability of its neighboring patches labeled as tumor can be relatively higher [24]. In fact, there are researches suggesting that the distribution of labels in pathology images has certain underlying structure proved to be beneficial to diagnosis [25]. However, some existing methods do not take the contextual information on neighboring labels into consideration. For example, some traditional binary classifiers like Support Vector Machine (SVM) and Maximum Entropy only consider one single input and ignore the spatial relationship with other inputs while predicting the labels [8]. Besides, the advanced DL model Convolutional Neural Network (CNN) also has this problem. Although the CNN has a large amount of input images, the spatial dependencies on patches are usually neglected and the inference is only based on the appearance of individual patches [26]. Hence, the structural model is proposed to solve this problem, and the most prevalent models are the MRFs and the CRFs, which explicitly model the correlation of the pixels or the patches being predicted [27]. Better results can be obtained when the information from the neighboring patches is integrated in the use of the MRFs or the CRFs. By incorporating them into the CNNs, the small spurious regions like noisy isolated predictions in the original output are almost eliminated [28]. Meanwhile, the boundaries are proved to be refined and become smoother [29].

As far as we know, there exists some survey papers related to medical image analysis and random fields. Among those studies, some survey [8] focuses on the CRFs and their application for different area. Some surveys [7], [30] concentrate on image analysis with random field models. However, those papers rarely refer to medical image analysis, let alone pathology image analysis. Additional papers direct on Artificial Intelligence in pathology image analysis [31], [32], such as using DL algorithm [33]–[35] and other image analysis techniques [36], [37]. Those papers introduce various algorithms or models, but the literature quantity about random field models is too limited to discuss them specifically, which is inconsistent with their importance. In the following paragraph, eleven of the reviews is listed and analyzed in detail.

He *et al.* [36] publishes a research survey in 2012, present-

ing an overview of image analysis techniques in the field of histopathology, especially for automated carcinoma detection and classification. This paper also introduces the MRFs in a separate paragraph. However, this paper refers to around 158 related works, only including seven papers related to the MRFs or CRFs.

Wang *et al.* [30] in 2013 provides a comprehensive summary of MRFs in computer vision and image understanding, and they summarize over 200 papers based on the MRFs. Among them, only seven papers focus on medical images, and no paper is related to pathology image analysis.

Irshad *et al.* [38] in 2014 summarizes the major trends from an exhaustive overview of various nuclei detection, segmentation, and classification techniques used in histopathology imagery. In summarizing table, there are around 100 papers on various image analysis techniques. Among them, there are only two related works using random field models.

Xing *et al.* [37], in 2016, gives a review concentrating on the recent state-of-art nucleus/cell segmentation approaches on different types of microscopy images. In the study, they summarize the CRF models in microscopy image analysis in a separate subsection. This review consists of a total of 326 papers, and mainly three papers employ the CRF models for image classification.

Litjens *et al.* [33] presents an overview of DL in medical analysis in the year of 2017. This paper provides overviews in a full range of application area, including neuro, retinal, digital pathology and so on. It summarizes over 300 contributions on various imaging modalities. Among them, twelve papers are relate to random field models.

Chang *et al.* [31] in 2018 exhibits a survey article based on recent advances in artificial intelligence applied to pathology. In this paper, around 73 related works are summarized, but there is only one paper related to the CRFs.

Wu *et al.* [7], in 2019, reviews several modern image labeling methods based on the MRFs and CRFs. In addition, they compare the result of random fields with some classical image labeling methods. However, they give less priority of pathology images. Among 28 papers summarized, only one paper focuses on medical image analysis and no paper is related to pathology images.

Wang *et al.* [34] publishes a survey in 2019, which focuses on the pathology image segmentation process using DL algorithm. In this review, the detailed process of whole image segmentation is described from data preparation to post-processing step. In the summary survey, there is only one paper based on random field models.

Yu *et al.* [8], in 2019, exhibits a new survey article presenting a comprehensive review of different versions of the CRF models and their applications. This paper classifies application fields of the CRFs into four categories, and discusses their application directions in biomedicine separately. There are 37 papers summarized in that subsection. However, only 20 of them concentrate on medical images, and two of them relate to pathology images.

Li *et al.* [32], in 2020 presents a review of cervical histopathology image analysis using machine learning methods. In this review, various machine learning methods are

discussed grouped by the application goals. Only two papers using novel multilayer hidden conditional random fields (MHCRFs) are included.

Rahaman *et al.* [35], in 2020, gives a review concentrating on cervical cytopathology image analysis using DL methods. A research (one of 178) focuses on a local FC-CRF combined with the CNNs is described specifically in application in segmentation part.

Besides the review paper mentioned before, there are some other survey papers in related field, e.g., the works of Li *et al.* [4]; He *et al.* [39]; Komura *et al.* [40].

From the existing survey papers mentioned above, it can be found that many researchers pay attention to pathology image analysis, or random field models application in the image analysis field. However, there is not a special paper that focuses on pathology image analysis using the MRF and CRF models. Hence, this comprehensive survey paper is presented to review all the related work in the past decades. In this survey, near to 40 related works are summarized from 2000 to 2019. Fig. 1 reports the increasing popularity of random field models overtime for the analysis of pathology images.

From 2002 to 2008, the number of research working on the MRFs increased steadily, but the figure remained at low level. The figure of CRFs stayed zero over that period. After 2002, they all experienced a rapid upward trend. Compared to the papers focusing on the MRFs, that of CRFs grew more rapidly and exceeded its counterpart in 2017. Overall, the total number of the research papers saw a consistent rise throughout the period shown.

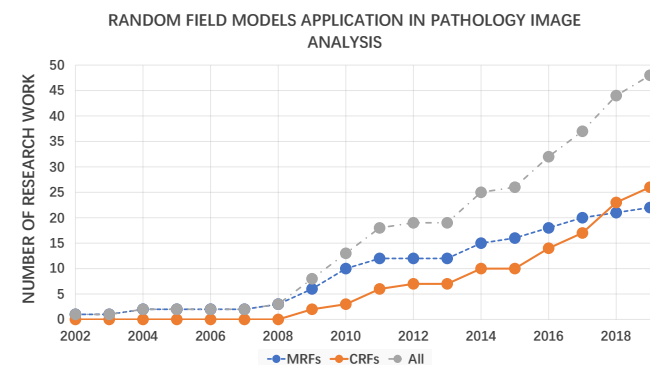


Fig. 1. Development trend for MRFs and CRFs applied in pathology image analysis.

From the papers that have studied so far, a general flow chart is given and shown in Fig. 2. It concludes the most popular methods in each step that have been used in pathology analysis.

E. Data Description

In the researches referred in this paper, some public retinal datasets are frequently used to prove the effect of the proposed method or make comparison between different approaches. Therefore, the detailed information of these datasets is concluded in Table I.

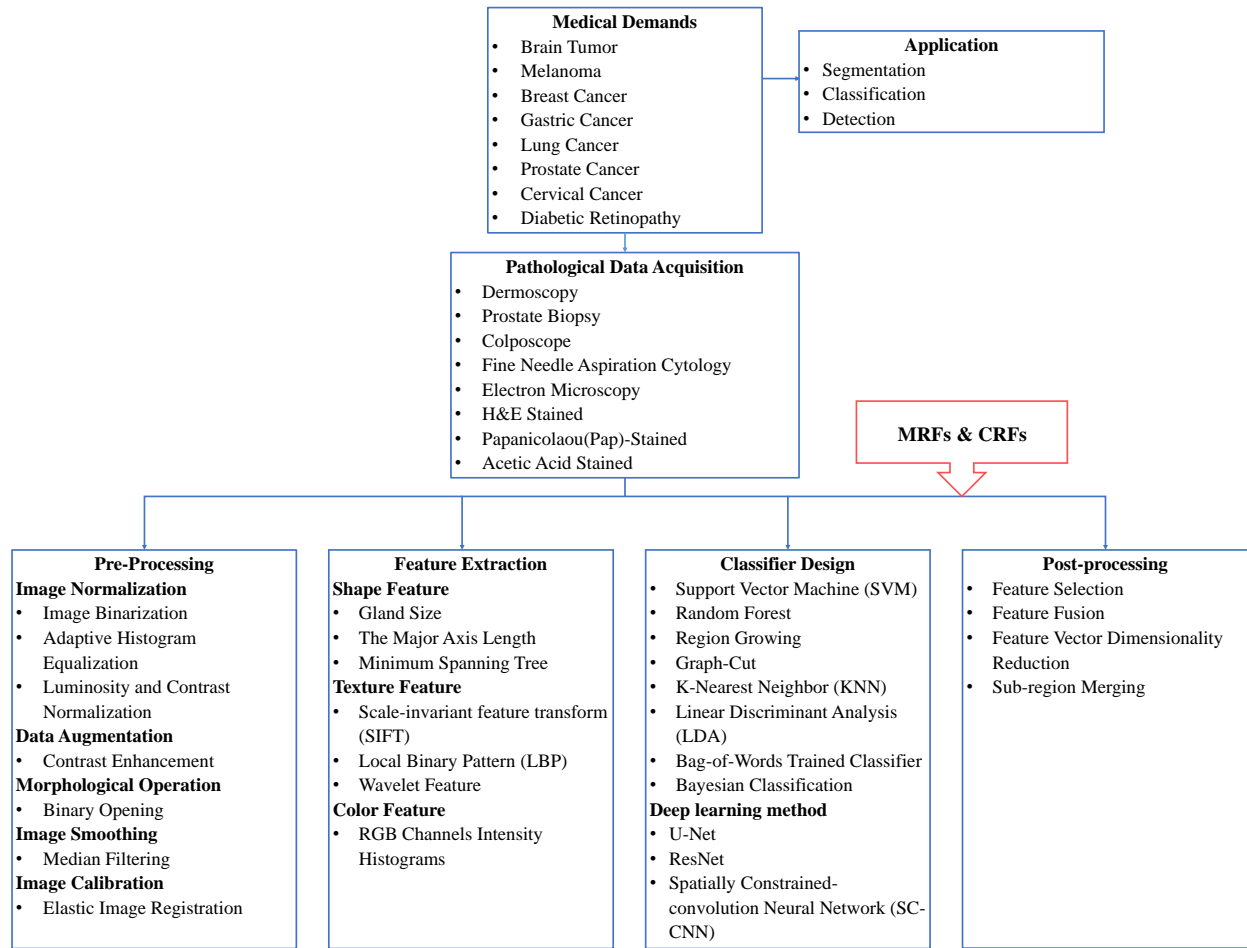


Fig. 2. General machine learning algorithm for pathology image analysis. It includes (1) Image acquisition, (2) Image pre-processing, (3) Feature representation, (4) Classifier design, (5) Image post-processing.

TABLE I
DETAILED INFORMATION OF FREQUENTLY-USED RETINAL DATASETS.

Datasets	Reference	Download Link	Dataset size	Resolution (pixels)
DRIVE	[41]	http://www.isi.uu.nl/Research/Databases/DRIVE/	40	565 × 584
STARE	[42]	http://cecas.clemson.edu/~ahoover/stare/	81	700 × 605
CHASEDB1	[43]	https://blogs.kingston.ac.uk/retinal/chasedb1/	28	1280 × 960
HRF	[44]	https://www5.cs.fau.de/research/data/fundus-images/	45	3304 × 2336
DRION	[45]	https://zenodo.org/record/1410497#.X1RFKMgzY2w	110	923 × 596
MESSIDOR	[46]	http://www.adcis.net/en/third-party/messidor/	1200	1440 × 960, 2240 × 1488 or 2304 × 1536

II. BASIC KNOWLEDGE

A. MRF

1) *Modeling*: Let the set $S = \{1, 2, \dots, N\}$ reference N sites to be classified. Each site $s \in S$ has two associated random variables: $X_s \in \Lambda \equiv \{\omega_1, \omega_2, \dots, \omega_L\}$ representing its state (class) and $Y_s \in \mathbb{R}^D$ indicating its D -dimensional feature vector. Particular instances of X_s and Y_s are denoted by the lowercase variables $x_s \in \Lambda$ and $y_s \in \mathbb{R}^D$. Let $\mathbf{X} = (X_1, X_2, \dots, X_N)$ and $\mathbf{Y} = (Y_1, Y_2, \dots, Y_N)$ refer to all random variables X_s and Y_s in aggregate. The state spaces

of \mathbf{X} and \mathbf{Y} are the Cartesian products $\Omega = \Lambda^N$ and $\mathbb{R}^{D \times N}$. Instances of \mathbf{X} and \mathbf{Y} are denoted by the lowercase variables $\mathbf{x} = (x_1, x_2, \dots, x_N) \in \Omega$ and $\mathbf{y} = (y_1, y_2, \dots, y_N) \in \mathbb{R}^{D \times N}$.

Let $G = \{S, E\}$ establish an undirected graph structure on the sites, where S and E are the vertices (sites) and edges, respectively. A neighborhood η_s is the set that contains all sites that share an edge with s , i.e. $\eta_s = \{r : r \in S, r \neq s, \{r, s\} \in E\}$. If P is a probability measure defined over Ω then the triplet (G, Ω, P) is called a random field. The probabilistic notations are simplified by omitting the random variables, e.g. $P(\mathbf{x}) \equiv P(\mathbf{X} = \mathbf{x})$ [2].

2) *Property*: The random field (G, Ω, P) is an MRF if its local conditional probability density functions (LCPDFs) satisfy the Markov property shown in Eq. (1):

$$P(x_s | \mathbf{x}_{-s}) = P(x_s | \mathbf{x}_{\eta_s}), \quad (1)$$

where $\mathbf{x}_{-s} = (x_1, \dots, x_{s-1}, x_{s+1}, \dots, x_N)$, $\mathbf{x}_{\eta_s} = (x_{\eta_s(1)}, x_{\eta_s(|\eta_s|)})$, and $\eta_i \in S$ is the i^{th} element of the set η_s . Thus, the Markov property simplifies the forms of the LCPDFs [47].

3) *Inference*: Given an observation of the feature vectors Y , the states X is to be estimated. The preferred method is an MAP estimation which entails maximizing the following quantity defined in Eq. (2) over all $x \in \Omega$:

$$P(x | y) = \frac{P(y | x)P(x)}{P(y)} \propto P(y | x)P(x) \quad (2)$$

The first term in Eq. (2) reflects the influence of the feature vectors. It can be simplified by assuming that all Y_s are conditionally independent and identically distributed given their associated X_s . This assumption implies that if the class X_s of site s is known then 1) the classes and features of the remaining sites provide no additional information when estimating Y_s and 2) the conditional distribution of Y_s is identical for all $s \in S$. As a result Eq. (3) is derived and shown as follows:

$$P(y | x) = \prod_{s \in S} P(y_s | x_s) = \prod_{s \in S} p_f(y_s | x_s), \quad (3)$$

The use of the single PDF p_f in Eq. (3) indicates that $P(y_s | x_s)$ is identically distributed across S . The second term in Eq. (3) reflects the influence of the class labels. In general, modeling this high-dimensional PDF is intractable. However, if the Markov property is assumed its formulation simplifies.

The connection between the Markov property and the JPDP of \mathbf{X} is revealed by the Hammersley-Clifford (Gibbs-Markovequivalence) theorem. This theorem states that a random field (G, Ω, P) with $P(\mathbf{x}) > 0$ for all $\mathbf{x} \in \Omega$ satisfies the Markov property if and only if it can be expressed as a Gibbs distribution in Eq. (4):

$$P(\mathbf{x}) = \frac{1}{Z} \prod_C V_C(\mathbf{x}), \quad (4)$$

where $V_C(\mathbf{x})$ is the potential function on the clique C and $Z = \sum_{\mathbf{x} \in \Omega} \prod_C V_C(\mathbf{x})$ is the normalization factor. A clique, C , in an undirected graph $G = (S, E)$ is a subset of the vertices, $C \subseteq S$, such that every two distinct nodes are adjacent [48].

B. CRF

Assuming \mathbf{Y} is a random variable over data sequences to be labeled, and \mathbf{X} is a random variable representing the corresponding label sequences. Let $G = (S, E)$ be a undirected

graph such that $\mathbf{X} = (\mathbf{X}_s)_{s \in S}$, so that X is indexed by the vertices of G . Then (\mathbf{X}, \mathbf{Y}) is a CRF in case, when condition on \mathbf{Y} , the random variables \mathbf{X}_s obey the Markov property mentioned before. Compared to the MRF model, a conditional model $p(\mathbf{X} | \mathbf{Y})$ from paired observation and label sequences, and not explicitly model the marginal $p(\mathbf{Y})$ [11]. The CRF can be represented by Eq. (5) as follows.

$$P(x | y) = \frac{1}{Z(y)} \exp\left(\sum_{i,k} \lambda_k t_k(x_{i-1}, x_i, y, i) + \sum_{i,j} \mu_j s_j(x_i, y, i)\right) \quad (5)$$

$$Z(y) = \sum_x \exp\left(\sum_{i,k} \lambda_k t_k(x_{i-1}, x_i, y, i) + \sum_{i,j} \mu_j s_j(x_i, y, i)\right)$$

In this form, t_k and s_j are the feature function relying on the positions, where t_k is the transition feature function defined on the edge which represents the features in the transfer from one node to the next node and relies on the current and previous positions, and s_j is the state feature function defined on a node which represents the features of a node and relies on the current position. λ_k and μ_j are learning parameters which is going to be estimated, and $Z(y)$ represents the normalization factor, where the summation is performed on all possible output sequences [8].

C. Optimization Algorithm

In this subsection, some representative optimization algorithms frequently used in the related works are introduced. Most of them are iterative models applied to estimate the observations from a given distribution.

1) *Expectation-maximization (EM)*: The mixture models such as random field models can be fitted by maximum likelihood via the EM algorithm where the data are absent. The algorithm takes initial model parameters as a priori and then estimates the missing data using the parameters. Once the complete data is obtained, the model parameters are estimated again by maximizing the expectation of likelihood. The algorithm involves two steps: (1) expectation step and (2) maximization step. At each step, the best estimate of the parameters is obtained, leading to the optimal data [49].

2) *Iterative conditional modes (ICM)*: ICM is a simple and iterative procedure which takes advantage of knowledge of the neighborhood system for MAP inference. The algorithm starts with an initial condition, either $P(X | Y)$ or a random selection. At each step, the algorithm tries to update the label at each site with the current, if new solution has the lowest energy. The algorithm converges when the energy for any site cannot be further decreased [50].

3) *Simulated Annealing*: Simulated Annealing is a classical technique for optimization. It simulates the process of annealing to find global minims or maxims from local minims or maxims [50].

III. MRFs

In this section, the related research papers focusing on pathology image analysis using the MRF models are grouped into two basic categories and surveyed, including application in segmentation and other tasks. Finally, a summary with method analysis is given in the last paragraph.

A. Image Segmentation using MRFs

In the research of tuberculosis disease, the quantification of immune cell recruitment is necessary. Considering that fact, in [51], an automatic cell counting method for histological image analysis consisting of color image segmentation is proposed. In this work, a new clustering approach based on a simplified MRF model is developed, which is called the MRF clustering (MRFC) method. It uses Potts model as a basic model, which is defined in eight connectivity using second order cliques and is able to handle both color and spatial information. They also complement the MRFC with a watershed on the binary segmentation result of aggregated zones (whose size is higher than a threshold value). This method uses seven groups of mouse lung slice images for testing and gets cell counting accuracy of 100% in a group containing 23 images.

In order to separate the nucleus and the cytoplasm regions from the blood cell images, which is an important task for hematologists and pathologists, a three-step image segmentation process is introduced in [52]. In the first step, an initial segmentation is completed using a Histogram Thresholding method. In the second step, segmentation with a Deterministic Relaxation, where the MAP criterion is formulated by the MRF, is adopted to smooth out the erroneous region in the last step. Finally, a separation algorithm consisting of four steps is used: boundary smoothing, detection of concavities, finding a pair of concavities to be connected, and the undoing the incorrect partitions. The proposed segmentation algorithm is applied to 22 cell images, including four basophils, three eosinophils, five lymphocytes, five monocytes, and five neutrophils, and it yields 100% correct results (some of the results are shown in Fig. 3).

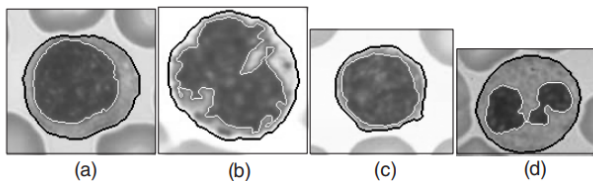


Fig. 3. Segmentation results with no touching rbc (white line on the boundary of nucleus, black line on the boundary of the cytoplasm): (a) Lymphocyte, (b) Basophil, (c) Lymphocyte, (d) Neutrophil. This figure corresponds to Fig.4 in original paper [52].

In [53], a couple method of the MRF and fuzzy clustering is adopted to express the adapt function and segment pathological images. In addition, particle swarm optimization (PSO) is added to the fuzzy clustering method. Thus, this model has the strong capability of noise immunity, quick convergence rate

and powerful ability of global search. On a 821-cell dataset, an accuracy value of 86.45% is finally achieved.

In [54], a quantitative CAD system is proposed to automatically detect and grade the extent of lymphocytic infiltration (LI) in digitized HER2+ breast cancer histopathology. Lymphocytes are automatically detected by a combination of region growing and the MRF algorithms first (the flow chart is shown in Fig. 4). Using the centers of individual detected lymphocytes as vertices, three graphs (Voronoi diagram, Delaunay triangulation, and minimum spanning tree) are constructed and features describing the arrangement of the lymphocytes are extracted from each sample. A nonlinear dimensionality reduction scheme is then used to project the high-dimensional feature vector into a reduced 3-D embedding space. Finally, an SVM classifier is used to discriminate samples with high and low LI in the reduced dimensional embedding space. In the first step, after Bayesian Modeling of LI via MAP estimation, the prior distribution $p(x)$ is defined by an MRF model, using ICM as optimization algorithm to assign a hard label to each random variable. Afterwards, each region is classified as either a breast cancer or lymphocyte nucleus. In this experiment, a total of 41 H&E stained breast biopsy samples at the Cancer Institute of New Jersey are tested, yielding an accuracy value of 0.9041.

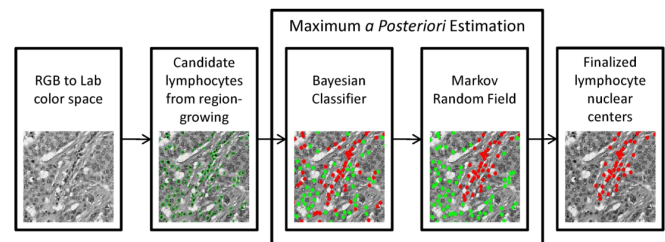


Fig. 4. Flowchart illustrating the main steps in the automated lymphocyte detection scheme. This figure corresponds to Fig.3 in original paper [54].

In [55], a four-step image segmentation process is employed to classify four categories of teratoma tissues. First, the image segmentation process is formulated in the Bayesian framework. Second, a hidden set of real-valued random fields determining the probability of a given partition are introduced, which reformulate the original segmentation problem in terms of real-valued hidden fields conditioning the random field and endowed with a Gaussian MRF (GMRF) prior promoting smooth fields. The distinctive features of this approach are that the original discrete optimization is converted into a convex program, thus much simpler to solve exactly using convex optimization tools. Thirdly, a form of isotropic vector total variation is adopted. Lastly, the Segmentation via a Constrained Split Augmented Lagrangian Shrinkage Algorithm (SegSALSA) is introduced to effectively solve the convex program which constitutes the marginal MAP inference of the hidden field. As Fig. 5 shown, the proposed system with SegSALSA finally yields an accuracy value of 0.84.

The morphology of the retinal blood vessel and the optic disk is an essential structural indicator that evaluates the presence and severity of many retinal diseases such as diabetic

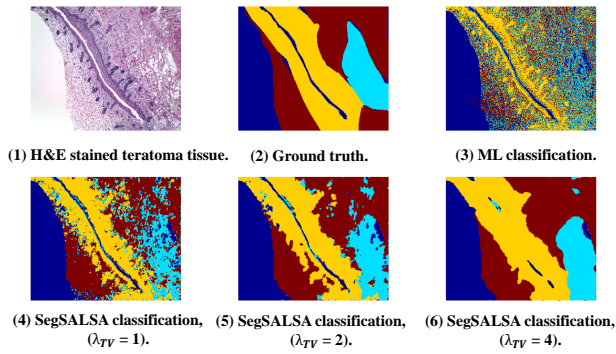


Fig. 5. H&E stained sample of teratoma tissue imaged at 40X magnification containing the following classes: background (dark blue), fat (light blue), mesenchyme (dark red), and skin (yellow). Top row: (1) original image, (2) ground truth, (3) ML classification (56% accuracy). Bottom row: (4) SegSALSA classification with $\lambda_{TV} = 1$ (73% accuracy), (5) SegSALSA classification with $\lambda_{TV} = 2$ (81% accuracy), (6) SegSALSA classification with $\lambda_{TV} = 4$ (84% accuracy). This figure corresponds to Fig.4 in original paper [55].

retinopathy (DR), hypertension, glaucoma and so on. Given that fact, in [56], an MRF image reconstruction method is applied to segment the optic disk. The extraction of the retina vascular tree using the graph cut technique is taken as the first step, so that the location of the optic disk can be estimated on the basis of the blood vessel. Afterwards, the MRF method is adopted to define the location of the optic disk, which eliminates the vessel from the optic disk region and meanwhile avoids the modification of other structures of the image. Fig. 6 (a) and (b) illustrate the optic disk segmentation results, compared with other prevalent methods. On the DRIVE dataset, an average overlapping ratio 0.8240, mean absolute distance 3.39, and sensitivity 0.9819 are finally achieved.

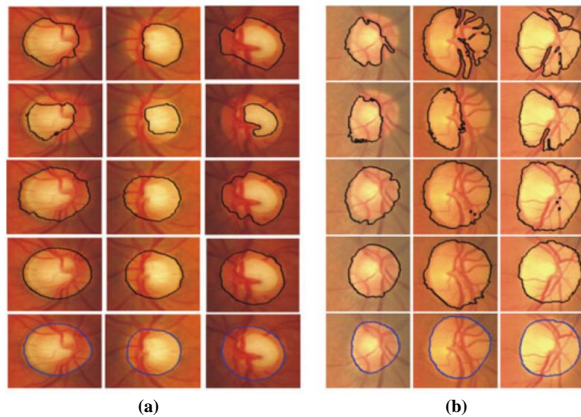


Fig. 6. (a) Optic disk segmentation results of DIARETDB1 images: first row topology cut, second row graph cut, third row compensation factor algorithm, fourth row MRF image reconstruction algorithm, and fifth row hand labeled. (b) Optic disk segmentation results of DRIVE images: first row topology cut, second row graph cut, third row compensation factor algorithm, fourth row MRF image reconstruction algorithm, and fifth row hand labeled. This figure corresponds to Fig.14 in original paper [56].

In [57], aiming to improve Melanomas early diagnosis accuracy, an overall process research based on dermoscopy images is proposed, including image noise removal, lesion region

segmentation, feature extraction, recognition of skin lesions and its classification. Lesion region segmentation is the first and essential step, where the image noise is removed first using contrast enhancement method, threshold and morphological method. In the main part, a fusion segmentation algorithm based on the MRF segmentation framework is proposed to improve the robustness of a single segmentation algorithm. The fusion strategy transforms the optimal fusion segmentation problem into the problem of minimizing the multi-dimensional space energy composed by the results of four segmentation algorithms (Statistical Region Merging, Adaptive Thresholding, Gradient Vector Flow Snake and Level Set). 1039 RGB images derived from two European universities are used for training and the overall process research finally achieves classification accuracy 94.49%, sensitivity 95.67% and specificity 94.31%.

Automated segmentation of nuclei is a significant step in breast histopathology quantitative image analysis. To detect the nuclei boundary, a four-stage procedure is proposed in [58]. In the preprocessing step, the enhanced grayscale images are obtained by applying principal component analysis to images. Second, the nuclei saliency map is constructed using tensor voting. Thirdly, the nuclei boundary is extracted by loopy belief propagation on the MRF model. In this stage, the most likely nuclei boundary is determined using a set of radial profiles of equal arc length intervals radiating from the center towards the edge of the window (shown in Fig. 7(a)). The MRF observable node variables are the intensity values from the nuclei saliency map in polar co-ordinate form, and the hidden node variables are nuclei boundary points on the radial profiles (shown in Fig. 7(b)). Finally, spurious nuclei are detected and removed after threshold processing. In a breast histopathology image containing 512 nuclei, the proposed system gets nucleus segmentation precision of 0.9657, recall of 0.7480 and Dice coefficient of 0.8830.

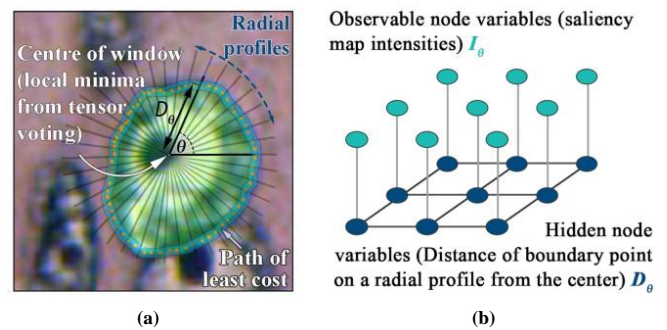


Fig. 7. a) Graphical illustration of boundary search paths. b) MRF formulation of the boundary delineation problem. This figure corresponds to Fig.5 in original paper [58].

In [59], a novel microaneurysms (MA) segmentation method based on the MRF is proposed to detect the first sign of DR in retina, where vessel network is first removed using a contrast enhancement method, then the MA candidates are extracted using local applying of the MRF, lastly an SVM classifier is designed to identify true MAs using a set of 23 features based on shape, intensity and Gaussian distribution of MAs intensity. Based on the purpose of our study, we

only focus on the MA candidate extraction approach. The EM algorithm is used to estimate the mean and variance in each class and the optimization of the main equation is done using a simulated annealing algorithm. But the MRFs have two limitations: Firstly, the number of the candidate regions after segmentation by the MRFs is so large that the false positive rate may increase; second, the size of some MAs might change so they cannot represent true MAs anymore. To overcome these limitations, region growing algorithm is used, where some regions are finally marked as non-MAs and removed from candidate regions. The authors manage to achieve an average sensitivity value of 0.82 on the publicly available database DIAREDB1.

In [60], a novel superpixel-based MRF framework is proposed for color cervical smear image segmentation, where the superpixels are generated by SLIC algorithm and 13-dimensional feature vector are extracted from each superpixel first, then initial segmentation result is provided by k -means++, lastly images are modeled as an MRF making the edges smoother and more coherent to semantic objects. An iterative adaptive classified algorithm (IACA) is applied for parameter estimation. Moreover, a gap-search algorithm is introduced to accelerate the iteration, which only updates the energy of necessary local regions, like the edge gap for refinement. The best results are achieved on Herlev public dataset, yielding 0.93 zijdenbos similarity index (ZSI) [61] of the nuclei segmentation.

In [50], an MRF-ANN framework is proposed to quantify the estrogen receptor (ER) scoring in breast cancer immunohistochemical images, where the white balancing is first applied to normalize the color image, then the MRF model with EM optimization is adopted to segment the ER cells. In addition, k -means clustering is applied to obtain the initial labels of the MRF model. Lastly, an artificial neural network (ANN) is subsequently used to obtain intensity-based score for ER cells from pixel color intensity features and the final ER score is computed by adding intensity and proportion scores (percentage of ER positive cells computed via cell counting) using a standard Allred scoring system. The proposed segmentation methodology is found to have F-measure 0.95 in 65 patients tissue slides obtained from the Tata Medical Centre, Kolkata, India.

In [62], a CAD approach is presented for identifying and classifying cancerous cell nuclei from pap-stained microscopic image of lung Fine Needle Aspiration Cytology (FNAC) sample, which is essential to lung cancer diagnosis. First, edge-preserving bilateral filtering is used for noise removal. Afterwards, Gaussian mixture model-based hidden Markov random field (GMM-HMRF) model is adopted for nucleus segmentation. Later, bag-of-visual words model is applied for nucleus classification, where scale-invariant feature transform features are extracted from segmented nucleus to train a random forest classifier model. In segmentation step, a hidden Markov random field (HMRF) as well as its Expectation Maximization (HMRF-EM) is employed to find out the unknown parameters in potential function. This algorithm needs morphological post-processing, including morphological opening operation, watershed algorithm and connected components

labelling method. The segmentation process yields a sensitivity and specificity value of 98.88% and 97.93%, respectively.

A two-level segmentation algorithm based on spatial clustering and the HMRFs is proposed in [63] to improve the segmentation accuracy of cell aggregation and adhesion region. First, k -means++ clustering is used to obtain the initial labels of the MRF based on color feature of pixels in the Lab color space. Second, the spatial expression model of the cell image is constructed by the HMRF, which considers the spatial constraint relation in order to reduce the influence of isolated points and smooth the segmentation area. Finally, the model parameters are optimized using the EM algorithm, and the label set is finally refined by the iterative algorithm. The experiment is based on the 61 bone marrow cell images from Moffitt Cancer Center, and after 10 iterations, the proposed method yields an accuracy value of 0.9685.

B. Other Applications using MRFs

1) *Prostate Cancer Detection from a US Research Team*: A joint research group from USA, leading by the researchers from Rutgers University and University of Pennsylvania, develops a serial work about Computer-Aided Detection of Prostate Cancer (CaP) on Whole-Mount Histology. These researches share almost the same procedure and the MRFs is mostly used in classification part, which shows exciting performance improvement.

In [64], a CAD algorithm is developed to detect the CaP in low resolution whole-mount histological sections (WMHSs). In addition to glandular features such as area, a highly indicative trait of cancerous glands is also their proximity to other cancerous glands. Therefore, the information in these glands are modeled using the MRF model. The CAD algorithm proceeds as follows: First, gland segmentation by region growing is performed on the luminance channel of a color H&E stained WMHS. Second, the system calculates morphological features for each gland and the features are then classified by Bayesian Classification, labeling the glands as either malignant or benign. Thirdly, the labels serve as the starting point for the MRF iteration, which then produces the final labeling. In this step, unlike most of the MRF strategies (such as the Potts model) which rely on heuristic formulations, a novel methodology are introduced, which allows the MRFs to be modeled directly from training data. The proposed system is tested in four H&E stained prostate WMHSs obtained from different patients, yielding a sensitivity and specificity value of 0.8670 and 0.9524, respectively, for cancerous area detection.

As an extension of this work, in [65], in order to solve the disadvantages of the tradition Random fields: Most of them produce a single, hard classification at a static operating point, the weighted maximum a posteriori (WMAP) estimation and weighted iterated conditional modes (WICM, a novel adaptation of ICM capable of WMAP estimation on RFs) are introduced. The use of these two algorithms prove to have good performance in 20 WMHSs from 19 patients images.

Based on the work above, in [47] and [66], the probabilistic pairwise Markov models (PPMMs) are presented. Compared to the typical MRF models, PPMMs, using probability distributions instead of potential functions, have both more intuitive

and expansive modeling capabilities. In Fig. 8, an example of the WMHS image detection steps is shown. In the experiment in [47], 20 prostate histological sections taken from 19 patients at two separate clinics (University of Pennsylvania and Queens University in Canada) are used for testing, the sensitivity (specificity is held fixed at 0.82) and area of the ROC curve (AUC) of the PPMMs increase to 0.77 and 0.87, respectively (compared to 0.71 and 0.83 using Potts model).

In [66], as a supplement, a comprehensive, hierarchical algorithm is expected, which quickly detects the cancerous regions at lower resolutions, and then refines and ultimately Gleason grades these regions at higher resolutions. 40 H&E stained histological sections from radical prostatectomies obtained from 20 patients in the same hospitals are tested, achieving a CaP detection sensitivity and specificity of 0.87 and 0.90 in the detection step.

It is also found that most such systems restrict the MRF performance to a single, static operating point (a paired sensitivity/specificity). To address this problem, in [67], weighted maximum posterior marginals (WMPM) estimation is developed, whose cost function allows misclassifications associated with certain classes to be weighted more heavily than others. Realizing WMPM estimation requires estimates of the posterior marginal distributions. The most prevalent means for estimating these is Markov chain Monte Carlo (MCMC) method. To more accurately estimate the posterior marginals, an equally simple but more effective extension of the MCMC method called EMCMC is also developed. The dataset consists of 27 digitized H&E stained histological sections from RPs obtained from 10 patients. Through quantitative comparison of ROC Curves using E-MCMC and other MCMC methods, the experiment proves better performance of the proposed method.

Based on the work above, a system for detecting regions of CaP using the color fractal dimension (CFD) is established in [68]. The tradition CFD algorithm is modified, which analyzes the red, blue and green channels in histology separately so that the most suitable bounding size of the hyper-rectangle can be found for each channel. And then, the authors combine the probability map constructed via CFD with the PPMM introduced in the above research. In the experiment, an AUC of 0.831 is achieved using 27 H&E stained histological sections from radical prostatectomies obtained from 10 patients at the University of Pennsylvania.

Their groups work also involves two researches focusing on automated segmentation methods. In [69], an MRF driven region-based active contour model (MaRACel) is presented for medical image segmentation. The shortcoming of most Region-based Active Contour (RAC) models is that it assumes every spatial location in the image is statistically independent of the others. Considering that fact, an MRF prior is incorporated into the AC model to utilize the valuable contextual information. 200 images obtained from H&E stained prostate biopsy samples are used for testing, yielding an average sensitivity, specificity, and positive predictive value of 71%, 95%, 74%, respectively. Fig. 9 shows segmentation results comparison between the proposed method and other methods.

In [70], the preliminary work is extended. The authors

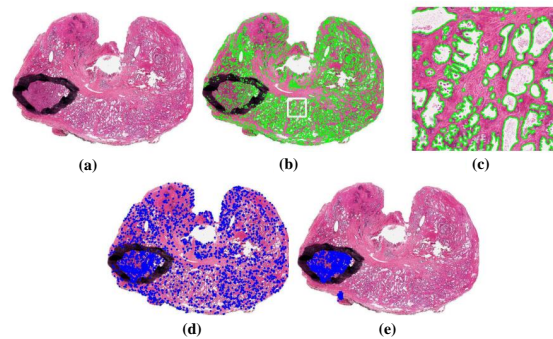


Fig. 8. (a) H&E stained prostate histology section; black ink mark provided by pathologist roughly indicates CaP extent. (b) Gland segmentation boundaries. (c) Magnified view of white box in (b). Centroids of cancerous glands before (d) and after (e) MRF iteration. This figure corresponds to Fig.3 in original paper [47].

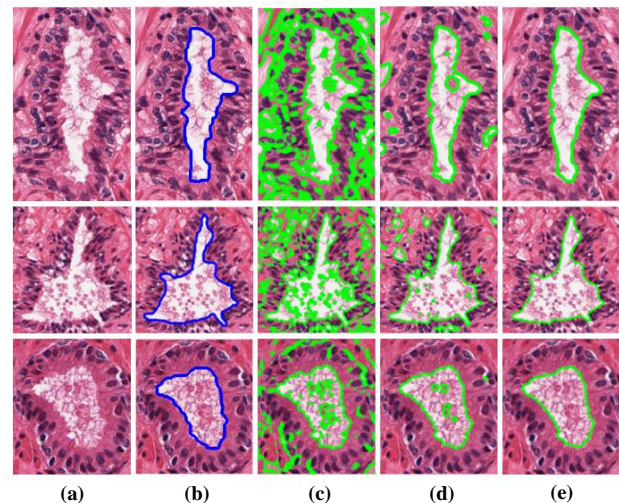


Fig. 9. Qualitative segmentation results for prostatic glands in digitized biopsy samples.(a) original images; (b) manual segmentations of the glandular boundaries (in blue); segmentation results (in green) for (c) Chan & Vese model, (d) Rousson and Deriche model and (e) MaRACel. This figure corresponds to Fig.2 in original paper [69].

introduce a method for incorporating an MRF energy function into an AC energy functional—an energy functional is the continuous equivalent of a discrete energy function. The MaRACel is also tested in the task of differentiation of Gleason patterns 3 and 4 glands (the flowchart is shown in Fig. 10), beside the segmentation of glands task. The proposed methodology finally gets gland segmentation Dice of 86.25% in 216 images and Gleason grading AUC of 0.80 in 55 images obtained from 11 patient studies from the Institute of Pathology at Case Western Reserve University.

2) *Other Research Teams*: For the purpose of assisting pathologists in correctly classifying meningioma tumors with a significant accuracy, a series of texture features extraction and texture measure combination methods are introduced in [71]. A Gaussian Markov random field model (GMRF) for third order Markov neighbors is used and seven GMRF parameters are estimated using the least square error estimation method. The diagnostic tumor samples (a set of 80 pictures) are derived

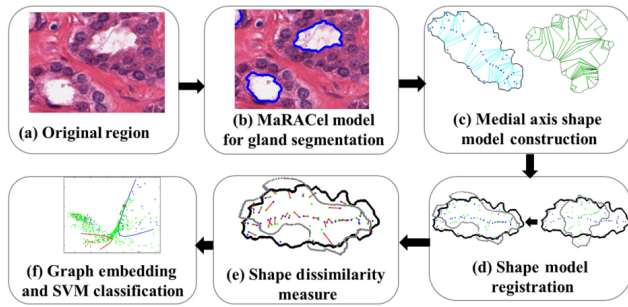


Fig. 10. The flowchart of automated gland segmentation with MaRACel model and ESDs for Gleason grading. This figure corresponds to Fig.1 in original paper [70].

from neurosurgical resections at the Bethel Department of Neurosurgery, Bielefeld, Germany. The combined GMRF and run-length matrix texture measures are proved to outperform all other combinations (e.g. Co-occurrence matrices, fractal dimension *et al.*) in terms of quantitatively characterizing the meningioma tissue, achieving an overall classification accuracy of 92.50%.

In [72]–[74], a hierarchical conditional random field (HIECRF) model based gastric histopathology image segmentation method is proposed to localize abnormal (cancer) regions. The post-processing step is based on the MRF and morphological operations for boundary smoothing as well as noise removal. The detail information of HIECRF will be discussed in next section.

C. Summary

A summary of the MRF methods for pathology image analysis is exhibited in Table II. This table comprises of some essential attributes of any research paper. Each row indicates publication year, reference, research team, input data, disease, data preprocessing, segmentation and classification techniques, and the result of an individual paper. From the table, it can be perceived that MRFs has a wide range of application in various disease detection, and mostly used in diagnosis of CaP and eye disease. Histopathology images are the most common input data, cytopathology images followed. Among these researches, the MRF models are applied in segmentation and classification tasks in most cases, and they are also used for postprocessing in [72] and feature extraction in [71]. Besides, with the development of MRF theory, some researchers propose the improvement or variants of the model, such as PPMM, GMRF and Connecting MRF, whose modeling capabilities are both more expansive than the typical MRF models. Moreover, feature extracted algorithm for classification is more complex over a period of 20 years. Since 2015, advanced machine learning models (SVM, ANN, Random Forest *et al.*) have been integrated into related research serving as classifiers, and the final results are significantly improved in larger dataset compared to those who use Bayesian classifier.

IV. CRFs

In this section, unlike the MRFs concluded before, it is known that the CRFs take segmentation and classification

tasks simultaneously. Instead, these researches are categorized into microscopic images and micro-alike (close-up/macro images) two images analysis work by the property of the input dataset. Their main differences can be concluded into two points: magnification and application scenarios. Most of the work to obtain micro-alike image can be accomplished within the magnification range of $2\times$ to $15\times$, such as endoscopy and ophthalmoscopy. On contrary, $20\times$ and $40\times$ optical magnifications are most frequently used for acquiring microscopic images, such as examining tissues and/or cells under a microscope for cancer diagnosis. Due to their different property, they are used in different application scenarios. Take colposcope as an example, lower magnification yields a wider view and greater depth of field for examination of the cervix. More magnification is not necessarily better, since there are certain trade-offs as magnification increases: the field of view becomes smaller, the depth of focus diminishes, and the illumination requirement increases [76]. When examining cells and tissues removed from suspicious lumps and bumps, and identifying whether they are from tumor or normal tissue, microscope of high magnification is indispensable.

The related research papers are concluded first. Finally, a summary with method analysis is given in the last paragraph.

A. Microscopic Images

In [77], a method based on multispectral data is proposed for cell segmentation. A CRF model incorporating spectral data during inference is developed. The loopy belief propagation algorithm is applied to calculate the marginal distribution, which also solves the optimal label configuration problem. The proposed CRF model achieves better results because the spectral information describing the relationship between neighboring bands helps to integrate spatial and spectral constraints within the segmentation process. 12 FNA samples are used for testing, and the result shows that the CRF model could help to get over segmentation difficulties when the contrast-to-noise ratio is poor.

In [78], a method is proposed for identifying disease states by classifying cells into different categories. Single cell classification consists of three steps: (i) cell segmentation with level sets and marker-controlled watershed algorithm, (ii) cell feature extraction with wavelet packets, and (iii) cell classification using SVM and CRF. The image information is represented in a CRF, since the features and distributions of the neighboring cells are of great importance for tissue cell classification. Its potential is related to the output discriminant value of SVM. After initialization of the CRF, considering that majority of cells (or nuclei) do not have a regular distribution over the tissue, an algorithm is presented to determine the optimal graph structure based on the local connectivity. This method is tested in lung tissue images containing 9551 cells, yielding specificity 96.52%, sensitivity 48.30%, and accuracy 90.26%.

In [79], a novel method is presented for detecting glandular structures in microscopic images of human colon tissues, where the images are transformed from Cartesian space to polar space first, then a CRF model (shown in Fig. 11) is

TABLE II

SUMMARY OF REVIEWED WORKS FOR PATHOLOGY IMAGE ANALYSIS USING MRFs. (SENSITIVITY (SN), SPECIFICITY (SP), AREA OF THE ROC CURVE (AUC), PRECISION (P), RECALL (R), ACCURACY (ACC), POSITIVE PREDICTIVE (PP), OVERLAPPING RATIO (ORATIO), MEAN ABSOLUTE DISTANCE (MAD), DICE (D), DICE COEFFICIENT (DC), F-MEASURE (F), ZIJDENBOS SIMILARITY INDEX (ZSI)).

Year, Ref, Research team	Disease	Input data	Task	Random field type	Optimization techniques	Feature extraction	Classification	Result evaluation
2002, [51], Meas-Yedid <i>et al.</i>	–	Mouse lung slice, 23 images	Segmentation (cell nuclei, immune cells and background), Immune cell counting	MRF	–	–	–	Acc=100%.
2004, [52], Won <i>et al.</i>	–	Blood cell, 22 images	Segmentation (nucleus, cytoplasm, red blood cell, and background)	MRF	Deterministic relaxation	Smoothness constraint and high gray level variance	–	Acc=100%.
2008, [64], Monaco <i>et al.</i>	CaP	4 WMHSs	Identification and segmentation of regions of CaP	MRF	ICM	Square root of gland area	Bayesian classification	Sn=86.7%, Sp=95.24%.
2009, [65], Monaco <i>et al.</i>	CaP	20 WMHSs	Identification and segmentation of regions of CaP	PPMM	WICM	Square root of gland area	Bayesian classification	–
2009, [47], Monaco <i>et al.</i>	CaP	20 WMHSs	Identification and segmentation of regions of CaP	PPMM	WICM	Square root of gland area	Bayesian classification	Sn=77%, Sp=82%, AUC=0.87.
2009, [53], Zou <i>et al.</i>	–	821 cells	Segmentation	MRF	FCM with PSO	–	–	Acc=86.45%.
2009, [54], Basavanthally <i>et al.</i>	Breast cancer	HER2+ H&E lymphocytes, 41 images	Identification and segmentation of regions of CaP	MRF	ICM	Voronoi diagram, Delaunay triangulation, and minimum spanning tree	Bayesian classifier, SVM	Acc=90.41%.
2010, [66], Monaco <i>et al.</i>	CaP	40 WMHSs	Identification and segmentation of regions of CaP	PPMM	WICM	Square root of gland area	Bayesian classification	Sn=87%, Sp=90%.
2010, [71], Al-Kadi <i>et al.</i>	Meningioma	Meningioma tumour, 80 images	Classification (malignant or benign)	GMRF	Least square error estimation	Fractal dimension, grey level co-occurrence matrix, grey level run-length matrix, GMRF	Bayesian classification	Acc=92.50%.
2010, [69], Xu <i>et al.</i>	CaP	200 prostate biopsy needle images	Segmentation of prostatic acini	MRF	–	–	–	Sn=71%, Sp=95%, PP=74%.
2011, [68], Yu <i>et al.</i>	CaP	27 WMHSs	Identification and segmentation of regions of CaP	PPMM	ICM	CFD	Bayesian Classification	AUC=0.831.
2011, [67], Monaco <i>et al.</i>	CaP	27 WMHSs	Identification and segmentation of regions of CaP	MRF	E-MCMC, M-MCMC	Gland area	WMPM classification	–
2014, [55], Bioucas-Dias <i>et al.</i>	Teratoma	Teratoma tissue, a 1600 1200 image	Classification of four categories of teratoma tissues	HMRF	EM based algorithm	–	–	Acc=84%.
2014, [56], Salazar-Gonzalez <i>et al.</i>	Eye disease	Fundus retinal images, DIARETDB1, DRIVE, STARE public dataset	Segmenting of blood vessel and optic disk	MRF	Max-flow algorithm	–	–	Oratio=0.8240, MAD=3.39, Sn=98.19% (in DRIVE).

Year, Ref, Research team	Disease	Input data	Task	Random field type	Optimization techniques	Feature extraction	Classification	Result evaluation
2015, [57], Liu et al.	Melanoma	Melanoma in Dermoscopy, 1039 images	Lesion region segmentation and classification (malignant or benign)	MRF	–	Symmetry, size, shape, maximum diameter, Gray level co-occurrence matrix, color features, SIFT	SVM classifier	Acc=94.49%, Sn=95.67%, Sp=94.31%.
2016, [58], Paramanandam et al.	Breast cancer	High-grade breast cancer images, 512 nuclei	Segmentation of the individual nuclei	MRF	Loopy Back Propagation	Tensor voting method	–	P=96.57%, R=74.80%, DC=88.3%.
2016, [59], Razieh et al.	Microaneurysms	Fundus retinal images, DIARETDB1 public dataset	Microaneurysms segmentation	MRF	Simulated annealing	Shape-based features, Intensity and color based features, Features based on Gaussian distribution of MAs intensity	SVM classifier	Sn=82%.
2016, [60], Zhao et al.	Cervical cancer	Color cervical smear images, Herlev and real-world datasets	Segmentation of cytoplasm and nuclei	MRF	Iterative adaptive classified algorithm	Pixel intensities and the shape of superpixel patches	–	Herlev: ZSI=0.93, 0.82; real-world: ZSI=0.72, 0.71 (cytoplasm, nuclei).
2017, [50], Mungle et al.	Breast cancer	Breast cancer immunohistochemical images, 65 patients tissue slides	ER scoring	MRF	EM, ICM and Gibbs sampler (with simulated annealing)	R, G and B values of individual cell blobs	ANN	F=96.26%.
2017, [70], Xu et al.	CaP	600 prostate biopsy needle images	Segmentation of prostatic acini and Gleason grading	Connecting MRFs	–	[75]	SVM classifier	Segmentation: D=86.25%, Gleason grading: AUC=0.80.
2018, [62], Dholey et al.	Lung Cancer	Papanicolaou-stained cell cytology, 600 image	Segmentation of the nucleus and classification (Small Cell Lung Cancer and Non-small Cell Lung Cancer)	GMM-HMRF	HMRF-EM	SIFT, <i>K</i> -Means Clustering, Construction of Visual Dictionary	Random Forest Training (Bag-of-Words)	Sn=98.88%, Sp=97.93%.
2019, [63], Su et al.	–	Bone marrow smear, 61 images	Segmentation	HMRF	EM	Color intensity	<i>k</i> -means	Acc=96.85%.

introduced to infer possible boundary of a gland and a visual feature based support vector regressor (SVR) is developed to verify whether the inferred contour corresponds to a true gland, finally the outputs of these two methods in the second step are combined to form the GlandVision algorithm ranking all the potential contours, and this generates the final results. In the inference process of the CRF, two chain structures are applied to approximate this circulate graph, which uses Viterbi algorithm to find the optimal results. The authors use the combination of cumulative edge map and the original polar image to generate the unary potential and the Gaussian edge potential as the pairwise potential. Besides, a thresholding is

performed to remove most of the false positives produced in this step. 10 microscopic images of human colon tissues are used for training and 10 images are used for testing, finally a segmentation accuracy of 0.732 is achieved (shown in Fig. 12). Based on the work above, in [80], a task called inter-image learning is introduced, which predicts whether those sub-images containing glands. A linear SVM is applied to tackle this problem, using the sum of the node potential of the CRF in contour detection task along with other mid-level features (listed in Table III in detail). This research also finds that all the gland contours proposed by the random field which rank according to the learned SVM score achieves the best

result compared to other index, so it is used as the final output of the CRF. Based on the same dataset, this method gets an accuracy of 80.4%. Beside the grey-scale images, it is also tested in 24 H&E stained images, yielding sensitivity 82.35%, specificity 93.08%, accuracy 87.02% and Dice 87.53%.

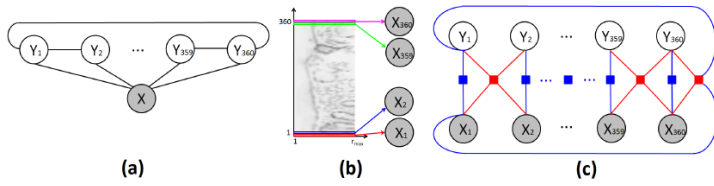


Fig. 11. After this transformation, a circular region with radius of r_{max} in the original image is transformed to a fixed size polar image of $360 \text{ rows} \times r_{max} - \text{columns}$. (a) The graphical model of the CRF containing 360 nodes; (b) Each row of the polar image is assigned a random variable; (c) The factor graph of the CRF model. This figure corresponds to Fig.2 in original paper [79].

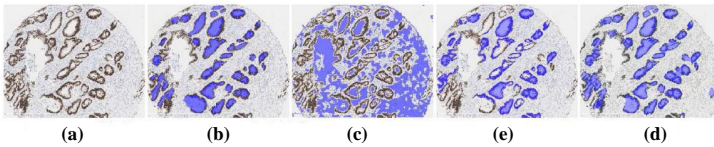


Fig. 12. Segmentation results of different approaches. (a) Original image; (b) Ground truth labeling; (c) (d) Results obtained by [81] and [82]; (e) Proposed method's result. Both [81] and [82] choose pixel or super pixel as the processing primitive, and they can hardly separate the 'gland' class from the 'background' class, whilst the object-based approach does a much better job. This figure corresponds to Fig.20 in original paper [79].

A system is presented to segment necrotic regions from normal regions in brain pathology images based on a sliding window classification method followed by a CRF smoothing in [29]. First, four features are extracted and encoded by Bag-of-words (BoW) algorithm. Then, an SVM classifier is applied in the sliding windows using the features extracted in the last step. Thirdly, the CRF model is applied to discard noisy isolated predictions and obtain the final segmentation with smooth boundaries. The node and edge potentials of the CRF is defined using the probability map provided by SVM. In 35 training data provided by the MICCAI 2014 digital pathology challenge, the proposed method gets a segmentation accuracy value of 0.66.

In [83], an end-to-end algorithm is proposed based on fully convolutional networks (FCN) for inflammatory bowel disease diagnosis to identify muscle and messy regions. In order to incorporate multi-scale information into the model, a specific field of view (FOV) method is applied. The architecture of multi-scale FCN is as follows: First apply various FCNs, each of which takes care of a different FOV in the input image; Then, the score maps produced by those FCNs are fused; Finally, fused score maps go through a soft-max function to compute a cross entropy classification loss. A CRF model is applied as a post-processing step after FCN to incorporate structural information, which uses the probabilities produced by FCN as its unary cost and also considers pairwise cost

bringing smoothness and consistency for label assignments. Tested in 200 H&E stained histology tissue whole slides, the authors manage to achieve an accuracy of 90%, region intersection over union (IU) of 56%.

The degree of deterioration of breast cancer is highly related to the number of mitoses in a given area of the pathological image. Considering that fact, a multi-level feature hybrid FCNN connecting a CRF mitosis detection model is proposed in [84]. On the open source ICPR MITOSIS 2014 dataset, the proposed classification methodology is found to have F-score 0.437.

In [85], a cell image sequence morphology classification method based on linear-chain condition random field (LCRF) is presented. Firstly, this problem is modeled as a multi-class classifier based on LCRF, a conditional probability distribution model assuming that X and Y have the same structure. Then, a series of features are extracted to describe the internal motion for cells image sequence, including deformation factor and dynamic texture. Lastly, the model parameter is estimated by discrimination learning algorithm called margin maximization estimation and the image sequence classification result is produced according to the input feature vectors. The effectiveness of the model is verified on micro image sequence data set of pluripotent stem cells from University of California, Riverside, USA, yielding an accuracy value of 0.9346.

In [86], a neural conditional random field (NCRF) DL framework is proposed to detect cancer metastasis in WSIs. The NCRF is directly incorporated on top of a CNN feature extractor (called ResNet) forming the whole end-to-end algorithm. Fig. 13 illustrates the overall architecture of the NCRF. Specifically, the authors use the mean-field inference to approximate marginal distribution of each patch label. Then, the network computes the cross-entropy loss and train the whole model with backpropagation algorithm. On the Camelyon16 dataset, including 270 WSIs for training, 130 tumor WSIs for testing, an average free response receiver operating characteristic (FROC) score of 0.8096 is achieved finally.

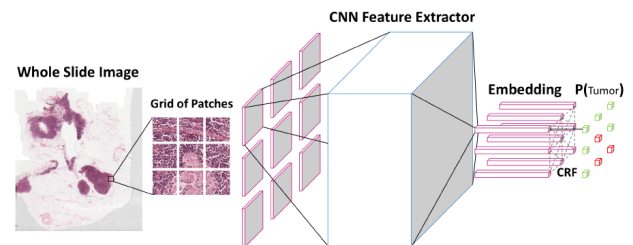


Fig. 13. The architecture of NCRF model. This figure corresponds to Fig.1 in original paper [86].

To recognize cancer regions of pathological slices of gastric cancer, a reiterative learning framework is proposed in [87], which first extracts regions of interest and subsequently trains the patch-based FCN followed by the overlapped region forecast and postprocessing operations with the FC-CRF. However, the performance of the CRF in their task is not satisfactory, because several erroneous data distributions in such weak

annotation task can cause the model to output worse results. On the gastric tumor segmentation dataset provided for the 2017 China Big Data and Artificial Intelligence Innovation and Entrepreneurship Competition, after adding the CRF to the model, a mean intersection over union Coefficient (IoU) value in test set decreases from 85.51% to 84.85%. Based on the work above, this research team improves the network structure, proposing a deeper segmentation algorithm deeper U-Net (DU-Net) in [88]. In this case, postprocessed with the CRF is proved to boost the performance and the IoU value increases to 88.4% in the same dataset.

A method using weak annotations for nuclei segmentation is proposed in [89]. Firstly, two types of coarse labels (the Voronoi label and cluster label) are generated using the points annotation image to derive complementary information. Second, label produced in last step is utilized to train a deep CNN model. The dense CRF is embedded into the loss function to improve the accuracy and further refine the model. In the experiment, lung cancer and MultiOrgan dataset are used for testing, both achieving accuracy over 98%. The result is shown in Fig. 14.

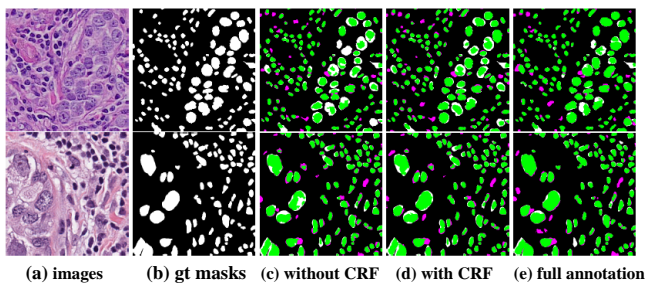


Fig. 14. Comparison of weakly and fully supervised training: (a) images, (b) ground-truth masks, (c)-(e) are results for weak labels without, with CRF loss and full labels, respectively, overlapped with ground-truth masks. Pixels in green, magenta, white are true positives, false positives and false negatives, respectively. This figure corresponds to Fig.4 in original paper [89].

A cell segmentation method using texture feature and spatial information is developed in [90]. In the first step, features are extracted and utilized to train machine learning model, providing pre-segmentation result. In the second step, the image is postprocessed by MRF and CRF model for binary denoising. The proposed segmentation methodology is tested in dataset from David Rimm Laboratory at Yale University and obtains F-score, Kappa and overall accuracy of 86.07%, 80.28% and 91.79%.

A novel multi-resolution hierarchical framework (called SuperCRF) inspired by the way pathologists perceive regional tissue architecture is introduced in [91] to improve cell classification. In single cell classification task, a Spatially Constrained Convolutional Neural Network (SC-CNN) is trained to detect and classify cells in high resolution (20) WSI into four categories: cancer cells, stroma cells, lymphocytes, and epidermis cells. Fig. 15(a) illustrates this network clearly. Then, a CRF, whose architecture is shown in Fig. 15(b), is trained by combining the cellular neighborhood with tumor region classification from low resolution images, given by the

superpixel-based machine-learning framework. Subsequently, the labels of the CRF single-cell nodes are connected to the regional classification results from superpixels producing the final result. Segmentation accuracy, precision and recall of 96.48%, 96.44%, and 96.29% are achieved on 105 H&E stained section images of melanoma skin cancer from The Cancer Genome Atlas (TCGA), shown in Fig. 15(c).

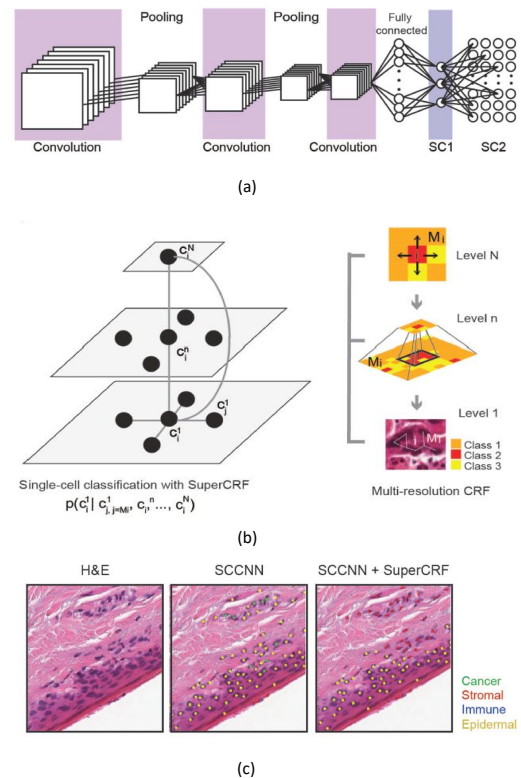


Fig. 15. Overview of the SuperCRF framework for analyzing H&E-stained pathological images of melanoma. (a)Graphical representation of node dependencies (cells and superpixels) across different scales. (b)Region classification scheme using a superpixel based machine-learning method in whole-slide images (5 and 1.25 magnification). (c)Representative results of the SC-CNN cell classifier alone and combined with the SuperCRF system. Note the misclassification of various stromal cells by the SC-CNN, which are corrected by the CRF model. This figure corresponds to Fig.1 in original paper [91].

In [72]–[74], a hierarchical conditional random field (HIECRF) model based gastric histopathology image segmentation method is proposed to localize abnormal (cancer) regions. The structure of the HIECRF model is shown in Fig. 16(a). Firstly, a DL network U-Net is retrained to build up pixel-level potentials. Meanwhile, the authors fine tune another three CNNs, including VGG-16, Inception-V3, and ResNet-50, to build up patch-level potentials. The binary potentials of their surrounding image patches are formulated according to the lattice layout described in Fig. 16(b)(c). When the HIECRF model is structured, graph-based post-processing is finally applied to further improve the segmentation performance. A segmentation accuracy of 78.91% is finally achieved on a public H&E stained gastric histopathological image dataset with 560 images.

In [92], a method based on a CNN is presented for

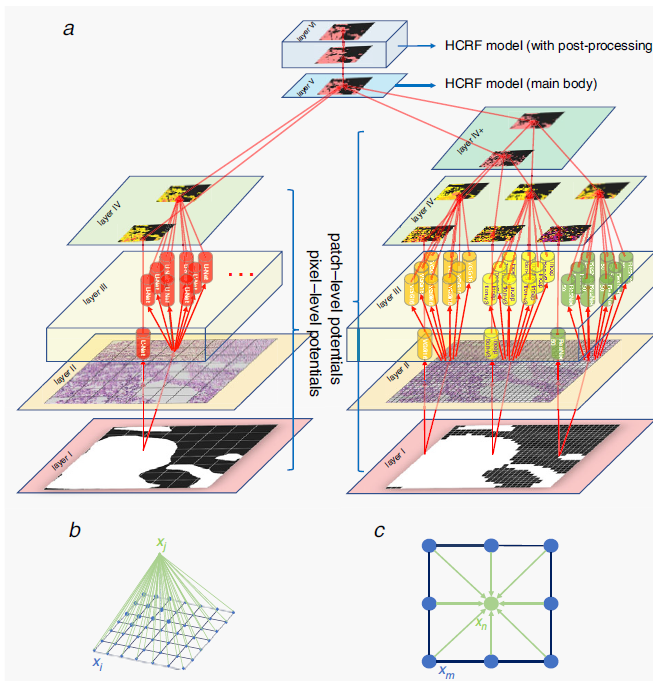


Fig. 16. Overview of HIECRF framework for analysing H&E stained gastric histopathological image (a) Structure of proposed novel HIECRF model. Left part denotes terms of pixel-level potentials, and right part shows terms of patch-level potentials; (b) 48 neighbourhood lattice layout of pixel-binary potential. Average of unary probabilities of 48 neighbourhood pixels is used as probability of pixel (central pixel in green); (c) Eight neighbourhood lattice layout of patch-binary potential. Average of unary probabilities of eight neighbourhood patches is used as probability of target patch (central patch in green). This figure corresponds to Fig.2 in original paper [72].

the objective of for automatic Gleason grading and Gleason pattern region segmentation of images with prostate cancer pathologies. An architecture that combines the atrous spatial pyramid pooling (ASPP) from Deeplab-V3 and the multiscale standard convolution inspired by a multiscale parallel branch convolutional neural network (MPB-CNN) is proposed and their feature maps are cascaded together to obtain initial segmentation results. Subsequently, a CRF-based postprocessing is applied to the prediction. The proposed system yielded an mIOU and overall pixel accuracy value of 0.773 and 0.895, respectively, for Gleason patterns segmentation.

A skin lesion segmentation ensemble learning framework based on multiple deep convolutional neural network (DCNN) models are proposed in [93]. The whole procedure can be divided as the following three steps: Firstly, multiple sheets of lesion segmentation is obtained from different pretrained DCNN models in training phase, then the unary potential is generated based on these segmentations as an input of the CRF models. Lastly, the CRF energy is minimized and yields the final prediction. In the experiment, ISIC 2017 [94] and PH2 [95] public datasets are used for testing, and a mean Dice coefficient of 94.14% is finally achieved.

A new framework that performs both segmentation and classification of skin lesions for automated detection of skin cancer is introduced in [96]. This framework contains two stages: In the first stage, an encoder-decoder FCN is applied to

learn the complex and inhomogeneous skin lesion features, and the output of the network is then sent into the post-processing CRF module which employs a linear combination of Gaussian kernels for its pairwise edge potentials is integrated for contour refinement and lesion boundaries localization. In the second stage, the segmentation result is classified by the FCN-based DenseNet into 7 different categories. The classification accuracy, recall and AUC scores of 98%, 98.5%, and 99% are achieved on HAM10000 dataset of over 10000 images.

B. Micro-alike images

An automated semantic image analysis method is proposed for cervical cancerous lesion detection based on colposcopy images in [97]. First, preprocessed images semantics are generated. k -means clustering is then applied to image segmentation. Thirdly, vessel structure features and statistical acetowhite features related to the optical properties of cervical tissues are extracted. In the final step, a CRF-based method classifies the tissue in each region (segmented in the second step) as normal or abnormal. The CRF-based classifier incorporates the classification results of neighboring regions produced by k -NN and LDA classifier in a probabilistic manner. Fig. 17 illustrates the proposed classifier designed for four tissue types based on the diagnostic features extracted. In the experiment, average sensitivity of 70% and specificity of 80% are achieved in detecting neoplastic areas on colposcopic images of 48 patients. As an extension of this work, the performance evaluation step is improved in [98]. It is clinically important to accurately locate the abnormal region and provide an overall diagnosis. Given that fact, a window-based approach for calculating sensitivity and specificity is proposed, where partition the image into disjoint windows first, then the classification result for each window is compared to the histopathology of the corresponding window in the histopathology image (ground truth). In the same dataset, compared with expert colposcopy annotations (AUC=0.7177), the proposed method gains better performance (AUC=0.8012). Fig. 18 shows examples of abnormal areas detected by proposed algorithm comparing the diagnostic accuracy with that of the colposcopist.

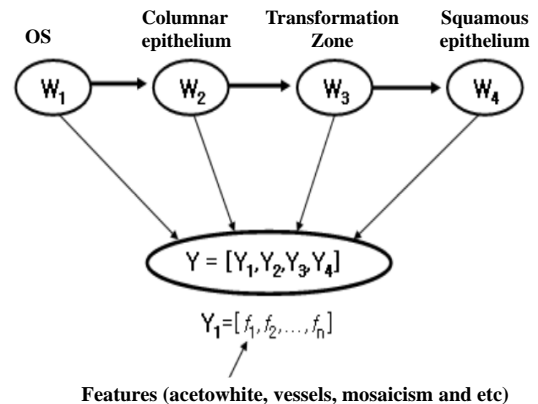


Fig. 17. Proposed CRF model design. This figure corresponds to Fig.1 in original paper [97].

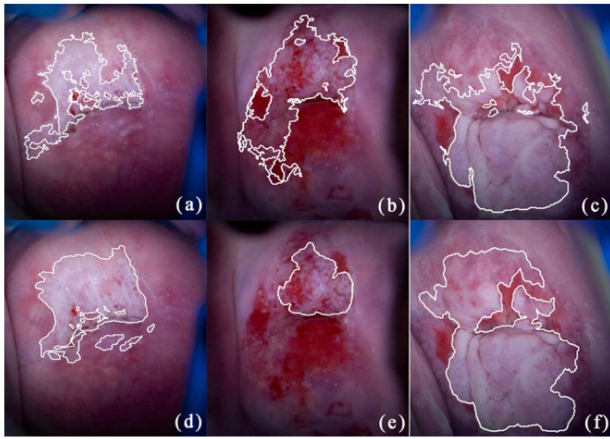


Fig. 18. Acetowhite region detection by proposed algorithm [(a)(c)] and the corresponding colposcopy annotations [(d)(f)]. This figure corresponds to Fig.9 in original paper [98].

In [99], a new approach is presented for segmenting vascular network into pathological and normal regions from only considering their micro-vessel 3D structure, where a distance map in preprocessed images is computed by calculating the Euclidean distance first, then the watershed of the inverse of the distance map is computed, finally a CRF model is introduced to label the watershed regions into tumor and nontumor areas. Key images in the whole process are shown in Fig. 19. This method is tested in real intra-cortical images obtained using synchrotron tomography imaging at the European Synchrotron Radiation Facility, which corresponds to the experts expectation.

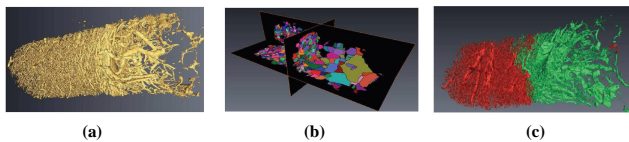
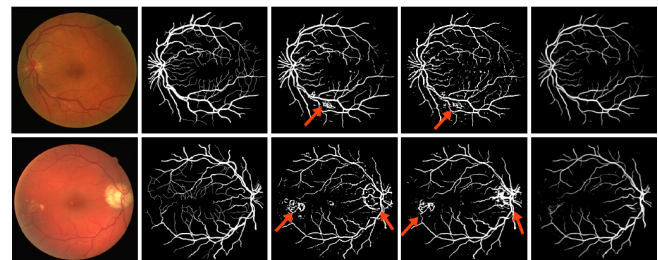


Fig. 19. (a)Volume rendering of the full volume of data after the merging step; (b) Watershed on the distance map opposite (c)Result: normal tissue (red) and tumor (green). This figure corresponds to Fig.1,3,6 in original paper [99].

In [100], a method is presented for blood vessel segmentation in fundus images based on a discriminatively trained FC-CRF model. Different from the tradition CRF, in the fully-connected version, each node is assumed to be a neighbor of every other. Following this approach, the method is able to consider not only neighboring information, but also long-range interactions between pixels. Firstly, some features (Gabor wavelets, line detectors *et al.*) are extracted, serving as the parameters of unary and pairwise energy combined with linear combination weight. Then, the parameters for unary and pairwise potentials are learned in a supervised way, using a Structured Output SVM (SOSVM). On the DRIVE dataset, this method yields sensitivity 78.5%, specificity 96.7%. As an extension of this work, a novel method based on the similar workflow is introduced in [101] to overcome a limitation of previous research: the configuration of the pairwise potentials of the FC-CRF is influenced by image resolution, because

it related to the relative distance of each pixel. In order to solve this problem, an approach, which is based on estimating the best parameters of feature parameters on a single data set and adapts them by multiplying them with a compensation factor, is developed. The authors manage to achieve over 96% accuracy and over 72% on DRIVE, STARE, HRF and CHASEDB1 four datasets.

In [102], a DL architecture is proposed to improve the performance of retinal vessel segmentation. Fully CNNs are utilized to generate a vessel probability map. Afterwards, an FC-CRF model is applied to build the long-range correlations between pixels to refine the segmentation result. Some of the unary and pairwise energy components are obtained by the vessel probability map. In the experiment, public dataset DRIVE and STARE achieve the segmentation accuracy of 94.70% and 95.45%. Furthermore, an improved system is introduced in [28]. An integrated deep network called DeepVessel is proposed, which contains four CNN stages and one CRF stage. A multi-scale and multi-level CNN with a side-output layer to learn a rich hierarchical representation is applied. The FC-CRF is applied in the last layer of the network, which is reformulated as an RNN layer so that can be utilized in the end-to-end DL architecture. Its unary and pairwise terms are determined by the previous layers and its loss function is combined with the CNN layer loss function minimized by standard stochastic gradient descent. DeepVessel is tested in three public databases (DRIVE, STARE, and CHASE DB1), yielding an accuracy value of 95.23%, 95.85% and 94.89%, respectively. The results comparison is shown in Fig. 19.



(A) Fundus image (B) Ground truth (C) Nguyen *et al.* (D) Orlando *et al.* (E) DeepVessel

Fig. 20. Retinal vessel segmentation results. Existing vessel segmentation methods (e.g., Nguyen *et al.* [103], and Orlando *et al.* [100]) are affected by the optic disc and pathological regions (highlighted by red arrows), while DeepVessel deals well with these regions. This figure corresponds to Fig.1 in original paper [28].

A four-step method is proposed for retinal vessel segmentation in [104]. Firstly, image preprocessing is applied for the noisy edges elimination and image normalization. Then, a CNN is properly trained to generate discriminative features for linear models. Thirdly, in order to reduce the intensity differences between thin and wide vessels, a combo of filters is applied to the green channel to enhance thin vessels. Finally, the dense CRF model is adopted to achieve the final retinal vessel segmentation, whose unary potentials are formulated by the discriminative features and pairwise potentials are comprised of the intensity value of pixel thin-vessel enhanced image. The flowchart of the whole process

is shown in Fig. 21. Among DRIVE, STARE, CHASEDB1 and HRF four public dataset, proposed method achieves the best result in DRIVE (F1-score= 0.7942, Matthews correlation coefficient (MCC)=0.7656, G-mean=0.8835).

An end-to-end algorithm is proposed in [105] to detect and segment red and bright retinal lesions, which are essential biomarkers of diabetic retinopathy (DR). A novel CNN architecture extending the U-Net with multi-task learning with patches is trained first. Then, segmentation outputs are refined with the CRF as RNN and the parameters of the kernels are trained with the rest of the network. The softmax output of each decoding module in CNN serves as the unary potential. The pairwise potential is formulated by a weighted sum of two Gaussian kernels. However, the result shows that the performance tends to get worse with the CRFs, for the reason that the CRFs could add tiny false positive red lesions, near the vessels. This method is finally evaluated on a publicly available DIARETDB1 database and obtains specificity value of 99.8% and 99.9%, for red and bright retinal lesions detection respectively.

In order to detect the optic disc in retinal image, an automatic method combining the CNN and CRFD is proposed in [106]. The first-order potential function of the CRF is constructed by CNN and the linear combination of Gaussian kernel is used to compose the second-order potential function. Finally, in postprocessing step, a regional restricts method is adopted to obtain the super-pixel area, which is used to analyze the consistency of the connected region labels. Afterwards, the result is refined by calculating the posterior probability mean of the super-pixel region. This method is verified on several retina databases and yields an accuracy of 100% in DRIVE, MESSID, DIARETDB, and DRION dataset. This method is improved and applied to other tasks like retina blood vessel segmentation and retina arteriovenous blood vessel classification in [107] by the same research team.

A precise segmentation of the optic disc method in fundus images is proposed in [108]. The input image is trained by modified U-Net or DeepLabV3 network, and the prediction is resized and fed to the CRF during training and inference. However, the CRFs are not easily GPU accelerated leading to slower performance after added. Moreover, because of the smooth ground truth masks with little sharp deformation and the already satisfying boundary produced by neural networks, the use of CRF added a very little boost in performance. No matter tested in private dataset or DRIONS-DB, RIM-ONE v.3, and DRISHTI-GS public dataset, Dice coefficient values all achieve over 95%.

C. Summary

A summary of the CRF methods for pathology image analysis is exhibited in Table III. The given index is composed of all the key attributes of any research paper. Each row designates publication year, reference, reasearch team, disease, onput data, task, inference algorithm, classifier, result evaluation. Similar to the MRFs mentioned before, the CRFs is also widely applied to a variety of diseases and mostly appears in segmentation and classification tasks. The mean-field approximation is the most common way to approximate

maximum posterior marginal inference, and further explanation will be given in Section V. Since 2016, DL network is applied on a wide range of computer vision tasks, including our reasearch area especially related to the CRFs. Hence, features are rarely extracted in an independent step, because the preprocessed image can be the input of DL method, which is more convenient. From the table, it can be noticed that most of the work achieves an accuracy of over 90%.

V. METHOD ANALYZE AND DISSCUSSION

A. Analysis of MRFs Methods

According to the researches on the MRF model applied in our field, it most frequently appears in segmentation task, and more specifically, plays two roles in most cases:

- It serves as a post-processing method to refine the initial segmentation result produced by classical segmentation methods;
- It is incorporated into other segmentation algorithms and they produce results together.

In the first case, the images are always segmented by some popular segmentation methods first to obtain initial labels, such as region growing, k -means, Bayesian classification, Otsu thresholding et al. However, most of these models do not consider contextual constraints, which are ultimately necessary in the interpretation of visual information [109]. Therefore, the MRF is applied based on the initial label using spatial dependencies, producing the final labeling. Compared to the second situation, initial segmentation is helpful to avoid the MRF algorithm falling into local optimal solutions, but it makes the whole process more complex. The papers involved in this article are [50], [52], [55], [63], [64]. In the second case, the MRF is employed in the popular segmentation methods mentioned above, solving the limitation in those methods assumptions. Hence, edges randomly occurring (due to noise) in the regions are much less likely to result in spurious boundaries and better performance can be achieved. The papers involved in this article are [62], [69].

The problems of parameter estimation and function optimization are crucial in the MRF paradigm. There are a few algorithms adopted to estimate the observations from a given distribution. Among them, EM and ICM are used most frequently. EM algorithm is an iterative algorithm for maximum likelihood estimation where the data are absent. Because of its simplicity as well as generality of the associated theory, it is broadly applicable these years [110]. However, the convergence of the EM algorithm can be painfully slow. The papers involved in this article are [50], [55], [62], [63]. The ICM algorithm uses the greedy strategy in the iterative local maximization. The convergence is guaranteed for the serial updating and is rapid, which can be an order of magnitude less than other popular methods [109]. The disadvantage is that different initial state leads to different results, which means the different modes of the MAP probability do not necessarily correspond to meaningful classifications. It seems to lack mathematical justification. The papers involved in this article are [50], [54], [64], [66]. In [65], this algorithm is improved to adapt the task requirement, which adds a parameter to

TABLE III

SUMMARY OF REVIEWED WORKS FOR PATHOLOGY IMAGE ANALYSIS USING CRFS. (SENSITIVITY (SN), SPECIFICITY (SP), AREA OF THE ROC CURVE (AUC), PRECISION (P), RECALL (R), ACCURACY (ACC), DICE (D), DICE COEFFICIENT (DC), F-MEASURE (F), MATTHEWS CORRELATION COEFFICIENT (MCC), FREE RESPONSE RECEIVER OPERATING CHARACTERISTIC (FROC), INTERSECTION OVER UNION COEFFICIENT (IOU), AGGREGATED JACCARD INDEX (AJI), MEAN INTERSECTION OVER UNION (MIOU), OVERALL PIXEL ACCURACY (OPA), MEAN OF ACCURACY (MAC), MEAN DICE COEF CIENT (MDC), MEAN JACCARD INDEX (MJJI), MEAN THRESHOLDED JACCARD INDEX (MTJI), MEAN BOUNDARY RECALL (MBR).)

Year, Ref, Research team	Disease	Input data	Task	Inference algorithm	Classifier	Result evaluation
2009, [77], Wu et al.	–	FNA cytological samples from thyroid nodules, 12 images	Segmentation (cell or intercellular material)	Loopy belief propagation	–	–
2010, [97], Park et al.	Cervical cancer	Colposcopy images, 48 patients	Segmentation, classification (normal or abnormal)	–	KNN, LDA	Sn=70%, Sp=80%.
2011, [98], Park et al.	Cervical cancer	Colposcopy images, 48 patients	Segmentation, classification (normal or abnormal)	–	KNN, LDA	AUC=0.8012.
2011, [78], Rajapakse et al.	–	Lung tissue, 9551 cells	Classification (benign cells or cancer cells)	–	SVM	Acc=90.26%, Sn=48.30%, Sp=96.52%.
2011, [99], Descombes et al.	Brain tumor	Micro-tomography vascular networks	Segmentation of vascular networks (normal or tumor)	Simulated annealing	–	–
2012, [79], Fu et al.	–	Human colon tissues, 1072 glands	Gland detection and segmentation	Viterbi algorithm	SVR	Acc=70.32%.
2014, [80], Fu et al.	–	Human colon tissues, 1072 glands; 24 H&E stained images, 333 glands	Gland detection and segmentation	Viterbi algorithm	SVM, SVR	Dataset 1: Acc=80.4%; Dataset 2: Sn=82.35%, Sp=93.08%, Acc=87.02%, D=87.53%.
2014, [29], Manivannan et al.	Brain tumor	Brain tissue, 35 images	Region Segmentation (necrotic regions or normal regions)	Graph cuts	SVM (Bag-of-words)	Acc=66%.
2014, [100], Orlando et al.	Eye disease	Fundus retinal images, DRIVE public datasets	Retinal vessel segmentation	Mean-field inference	SOSVM	Sn=78.5%, Sp=96.7%.
2016, [83], Wang et al.	IBD	Intestinal tissue, 200 images	Semantic segmentation (muscle or messy regions)	–	FCN	Acc=90%, IU=56%.
2016, [102], Fu et al.	Eye disease	Fundus retinal images, DRIVE, STARE public datasets	Retinal vessel segmentation	Mean-field inference	CNN	DRIVE: Acc=94.70%, Sn=72.94%; STARE: Acc=95.45%, Sn=71.40%.
2016, [28], Fu et al.	Eye disease	Fundus retinal images, DRIVE, STARE, and CHASE DB1 public datasets	Retinal vessel segmentation	Stochastic gradient descent	CNN	DRIVE: Acc=95.23%, Sn=76.03%; STARE: Acc=95.85%, Sn=74.12%; CHASE DB1: Acc=94.89%, Sn=71.30%.
2016, [101], Orlando et al.	Eye disease	Fundus retinal images, DRIVE, STARE, CHASEDB1 and HRF public dataset	Retinal vessel segmentation	SOSVM	–	DRIVE: Sp=98.02%, Sn=78.97%; STARE: Sp=97.38%, Sn=76.92%; CHASE DB1: Sp=97.12%, Sn=72.77%; HRF: Sp=96.80%, Sn=78.74%.
2017, [104], Zhou et al.	Eye disease	Fundus retinal images, DRIVE, STARE, CHASEDB1 and HRF public dataset	Retinal vessel segmentation	Structured support vector machine, fast inference	Modified version of MatConvNet	DRIVE: F1-score= 0.7942, MCC=0.7656, G-mean=0.8835; STARE: F1-score=0.8017, MCC=0.7830, G-mean=0.8859; CHASEDB1: F1-score=0.7644, MCC=0.7398, G-mean=0.8579; HRF: F1-score=0.7627, MCC=0.7402, G-mean=0.8812.

Year, Ref, Research team	Disease	Input data	Task	Inference algorithm	Classifier	Result evaluation
2017, [84], Wu et al.	Breast cancer	Breast cancer biopsy images, 1136 images	Mitosis detection	Error back propagation	AlexNet	F=43.7%.
2017, [85], He et al.	–	Pluripotent stem cells, 306 sequences	Morphological change pattern classification (healthy, unhealthy or dying)	Margin maximization estimation	LCRF	Acc=93.46%.
2018, [86], Li et al.	Breast cancer	WSIs, 400 images	Classification (normal or tumor)	Mean-field inference	ResNet-18 and ResNet-34	FROC= 0.8096.
2018, [87], Liang et al.	Gastric cancer	Gastric tumor tissue, 1400 images	Segmentation (normal or tumor)	–	FCN	IoU=85.51%.
2018, [88], Liang et al.	Gastric cancer	Gastric tumor tissue, 1400 images	Segmentation (normal or tumor)	–	DU-Net	IoU=88.4%.
2018, [105], Playout et al.	Diabetic retinopathy	Fundus retinal images, DIARETDB1 public dataset	Red and bright retinal lesions detection and segmentation	Adadelta algorithm	Modified version of U-Net	Red lesions: Sn= 66.9%, Sp=99.8%; bright lesions: Sn= 75.3%, Sp=99.9%.
2018, [106], Huang et al.	Eye disease	Fundus retinal images, DRIVE, STARE, MESSID, DIARETDB, DIARETD and DRION dataset	Optic disc identification	Mean-field inference	CNN	DRIVE, MESSID, DIARETDB, and DRION: Acc=100%; STARE: Acc=98.90%; DIARETD: Acc=99.90%.
2019, [89], Qu et al.	Lung Cancer	H&E stained histopathology images, lung cancer and MultiOrgan dataset	Nuclei segmentation	Mean-field inference	Modified version of U-net	Lung Cancer dataset: Acc=98.1%, F=92.6%, D=93.9%, AJI= 93.2%; MultiOrgan dataset: Acc=98.7%, F= 96%
2019, [90], Jamal et al.	–	Histopathological images, 58 images	Cellular segmentation	Iterated CRF	SVM, random forest, KNN	F=86.07%, Kappa=80.28%, Acc=91.79%.
2019, [91], Konstantinos et al.	Melanoma	Melanoma skin cancer, 105 images	Single-cell classification (cancer cells, lymphocytes, stromal cells or epidermal cells)	Stochastic gradient descent	SC-CNN	Acc=96.48%, P=96.44%, R=96.29%.
2020, [72] [74], Sun et al.	Gastric cancer	H&E stained gastric histopathological images, 560 images	Segmentation (normal or tumor)	–	CNNs	Acc=78.91%, P=41.58%, D=46.29%.
2020, [92], Li et al.	Prostate cancer	Prostate cancer tissue microarray, 1211 images	Gleason grading	–	ASPP and CNNs	mIOU=77.29%, OPA=89.51%.
2020, [108], Bhatkalkar et al.	Eye disease	Fundus retinal private dataset, 300 images	Segmentation of optic disc	–	DeepLabV3 et al.	DC=0.974.
2020, [93], Qiu et al.	Pigmented skin lesion	Dermoscopy images, ISIC 2017 and PH2 public dataset	Segmentation of skin lesion	Mean-field inference	DCNNs	mAC=96.20%, mDC=94.14%, mJI=89.20%, mTJI=68.10%.
2020, [96], Adegun et al.	Skin cancer	Dermatoscopic images, HAM10000 public dataset	Segmentation and classification of skin lesions	Mean-field inference	FCN-Based DenseNet framework	Acc=98.0%, F1-score=98.0%, R=98.5%.

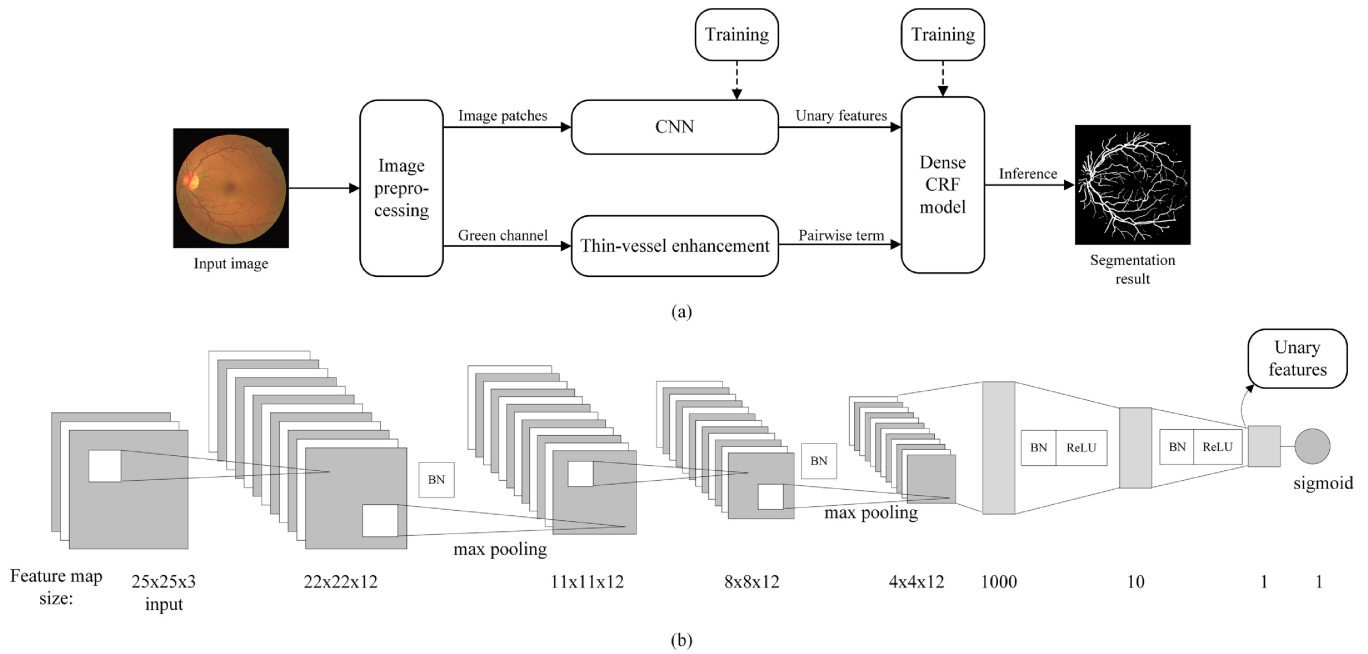


Fig. 21. Overview of the proposed method. (a) Flowchart of the proposed method. (b) Structure of the CNN used for discriminative feature learning (BNBatch Normalization layer, ReLU Rectified Linear Units). This figure corresponds to Fig.1 in original paper [104].

implicitly weight the importance of each class. The summary of the popular methods is shown in Fig. 22.

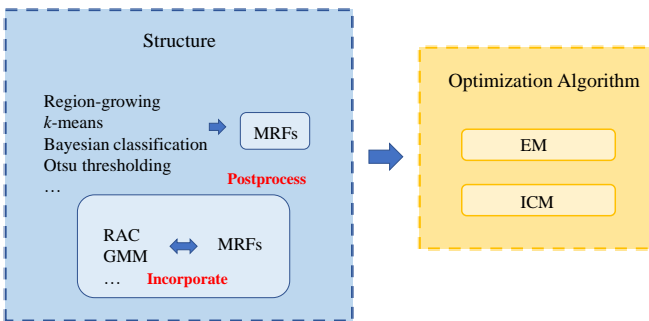


Fig. 22. The popular methods in MRFs for pathology analysis tasks.

B. Analysis of CRFs Methods

Nowadays, with the increasing attention of the CRF, various improvements have been developed, among which the FC-CRF (dense CRF) is the most frequently employed structure in the reviewed tasks, especially for the researches on eye diseases. The FC-CRF is a type of discriminative model, where each node is a neighbor of each other, so that contextual relations between different class labels or long-range dependencies can be modeled to make the edges smoother and more coherent to semantic objects [8] [7]. The papers involved in this article are [28], [84], [86], [87], [89], [100]–[102] et al. The FC-CRF improves the accuracy, but makes the inference process computationally expensive. To circumvent the limitation, the mean-field approximation, a highly efficient approximate inference algorithm for FC-CRF, is proposed and become the most common inference approaches in the reviewed papers. The mean-field approximation algorithm is

used to obtain the marginal label distribution of each patch, which is able to achieve significantly more accurate image-labeling performance and provide results in less than a second [111]. The papers involved in this article are [86], [89], [100], [102], [106].

Driven by the development of machine learning, from 2016, more and more researches integrate CRF into DL method, and they can be divided into two groups:

- The DL networks outputs form the CRF components, and approximate maximum posterior marginal is inferred by optimization techniques afterwards (such as [72], [102], [104]);
- Firstly, approximate marginal distribution of each patch label is computed using the inference algorithm. Then, the CRFs are embedded in the loss function of DL network and they are trained together to minimize the loss and achieve optimal labels. (e.g. [28], [83], [86], [105], or the CRF loss is used to fine-tune the trained model, e.g. [84], [89]).

The former applies the CRFs as a post-processing step after DL network to incorporate structural information. However, this does not fully harness the strength of CRFs since it is disconnected from the training of the DL network [112]. By contrast, the latter combines the DL network and CRF layers into an integrated DL architecture, which is an end-to-end learning method that reduces the complexity of the project. In [28], [83], [105], the CRFs is implemented as an RNN and plugged in as a part of a CNN, so the whole deep network can be trained end-to-end utilizing the back-propagation algorithm. The main advantages are as follows: First, DL network’s lack of spatial and appearance consistency of the labelling output resulting in poor object delineation and classification accuracy loss. CRFs can be used to overcome

this drawback, and this method combines the strengths of both of them. Second, although DL network can perform promising result, it has poor interpretability in mathematic theory [113]. However, DL network and CRF are convertible, so the CRF can be used to improve the interpretability of DL theory [112]. Therefore, the CRFs have a solid theoretical foundation and can be converted into DL network with good practical results. In conclusion, the CRFs has the dual advantages in theory and practice aspect, providing a unique perspective for pathology image analysis. The summary of the popular methods is shown in Fig. 23.

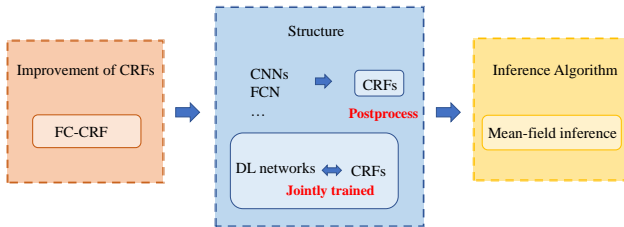


Fig. 23. The popular methods in CRFs for pathology analysis tasks.

C. The Potential Methods in Our Fields

In this subsection, we introduce some potential random field methods that have been successfully implemented in some other image analysis tasks and have potential in pathology image analysis as well.

1) *Potential Methods of MRFs*: With the continuous growth of image database, it is notably costly to create annotations associated with different combinations of imaging capabilities and regions of interest. The max-flow algorithm is frequently applied in the MRF problems. In [114], the theory that maximum a posteriori estimation of the image labels can be formulated as a capacitated max-flow problem over a continuous domain with unknown flow capacities is proposed. Through considering an MRF prior over the neighborhood structure in the image, the flow capacities are then iteratively obtained. Compared to other unsupervised methods, it achieves more than 90% improvement in terms of Dice score in brain tumor MR images segmentation task. In [115], an approach focusing on solving multi-atlas segmentation problem is proposed. The study reformulates it as an MRF energy optimization problem, and to optimize the arising MRF energy function, an efficient optimization scheme based on continuous max-flow is introduced. This method is evaluated in an MR dataset, yielding mean Dice coefficients of nearly 90%.

The max-flow technique can be calculated using a reliable, inherently parallelizable multiplier-based algorithm with guaranteed convergence, which makes it suitable for the optimization of large labelling problems [115]. Especially in some whole slide image analysis task, it is hopeful that the MRFs with Max-flow algorithm can be really helpful handling this kind of work.

2) *Potential Methods of CRFs*: Nowadays, with the increasing attention of the CRF, various improvements have been developed [8]. The multi-label CRF is one of them, which is

capable to mark one symbol with more than one label by using long-range interactions to encode contextual information. It can view nonadjacent tokens as an entity and simultaneously detect objects of different classes in image segmentation tasks [116]. To the best of our knowledge, there is no previous work using the multilabel CRF on pathology image analysis.

A multi-label CRF for semantic image segmentation task is proposed in [116], where each layer represents a single object class and is regularized independently. The label space context is modeled through long-range interactions between layers, where the sparse inter-layer connections penalize the unlikely occurrence of some groups of labels. They finally achieve the state-of-the-art performance on the MSRC-1 and the CorelB datasets. Moreover, in [117], a perturbation-based sampling approach for dense multi-label CRFs is introduced, which is computationally efficient and easy to implement. The method is validated on synthetic and clinical Magnetic Resonance Imaging data, achieving a promising result of the specificity value of 0.88 on the dataset containing 14 patients. Furthermore, an unmanned aerial vehicle (UAV) imagery classification problem is formulated within a multi-label CRF framework in [118]. Firstly, an opportune representation and a multilayer perceptron classifier are used to provide multilabel prediction probabilities in UAV image, which is subdivided into a grid of tiles. Second, the multilabel CRF model is applied to integrate spatial correlation between adjacent tiles as well as the correlation between labels within the same tile, aiming to iteratively improve the multilabel classification map. Outstanding performance achieves with 83.40% accuracy value.

In our field, most researches study only the binary classification of images such as cancer versus non-cancer. However, the categories to be classified are not always antithetical. For example, in [119], the whole slide breast histopathology images can be labeled as 5 classes (non-proliferative changes only, proliferative changes, atypical ductal hyperplasia, ductal carcinoma in situ and invasive carcinoma). So, it is believed that the multilabel CRF can show outstanding performance in our field, especially in histopathology image and colposcopic image analysis.

Another improved model of the CRFs is the hierarchical CRF (HIECRF) model, which belongs to the discriminative models and offers hierarchical and multilevel semantic. While inheriting the advantages of the CRF model, the HIECRF model achieves the integration of different scales of information [120] or the short-range interactions (e.g., pixelwise label smoothing) as well as the long-range interactions (e.g., relative configurations of objects or regions [121]). Some notable applications of the HIECRF for image classification problems are introduced below.

In [120], an HIECRF model is proposed for synthetic aperture radar image segmentation. The unary and pairwise potentials are constructed at each scale in order to capture the global and local image information from the perspective of multiresolution analysis. Besides, the mean-field approximation is employed to derive a hierarchical inference algorithm for the HIECRF model and provide the maximization of the posterior marginal estimate of the model. The proposed

method yields a segmentation accuracy value of 89%. Similarly, an associative HIECRF model is designed in [122] to improve the classification accuracy of high-resolution remote sensing images. The model is built on a graph hierarchy, where the pixel layer serves as a base layer and multiple superpixel layers are derived from a mean shift pre-segmentation. The potentials of the proposed model are defined based on clustered features of pixels for superpixels extracted at each layer. This method finally reaches an overall accuracy of 81.59%.

The characteristic of remote sensing imagery requires their analysis methods have the capacity to model multiscale object features and semantic information, thus reducing classification errors. It has shown that learning discriminative patterns from the multiscale features delivers a more robust classifier with better discriminant performance in pathology analysis [123], [124]. Maybe because it corresponds to the way that the pathologists diagnose diseases, by examining macroscopical features to microcosmic features. These arguments demonstrate the potential of the HIECRF method, which can be applied in our field especially in histopathology image analysis.

D. The Potential Methods in Other Fields

The MRF and CRF methodology discussed in this paper is not only applicable for the pathology image, but also can work in other image analysis fields, such as remote sensing images, computed tomography (CT) images, magnetic resonance imaging (MRI), and images collected by pipe robots. There are many CAD systems developed for high-resolution remote sensing image segmentation [125], [126]. The remote sensing images share the same rotating properties with cytopathology images, which are both without directivity. For example, SuperCRF in [91], which models nodes for cells and superpixels as well as edges whenever there is a spatial relationship between node by a CRF, is highly possible to apply for remote sensing image segmentation. Besides, the discussed segmentation algorithms also have potential applications in CT and MRI. In microaneurysms (MAs) detection tasks, there are two important difficulties, namely, nonuniformity of background intensity and the unequal amount of background pixels and MAs. Thrombus [127], [128] and pulmonary nodule [129] detection tasks also have these characteristics. Moreover, the geometric structure of the thrombus is irregular, which is similar to that of the optic disk. Thus, the MRF applied in [59] has a possibility to employ in these two fields. The instability of light in tunnels and cameras angle and distance from the surface are two serious problems when detecting images captured by pipe robot. Meanwhile, the endoscopic image analysis also meets this question [130], [131]. So, the CRF model proposed in [97], [98] can find significant use in this area. In conclusion, the methods of MRF and CRF summarized in this review can bring a new perspective to the research in other fields.

VI. CONCLUSION AND FUTURE WORKS

The MRFs and CRFs have drawn great attention of scholars in various research area since being proposed. This study reviews the recent research about the MRF and CRF models

applied in pathology analysis in the literature. Firstly, this paper presents an introduction of the random field models and pathology. Secondly, it elaborates on the both models background knowledge, including their property, modelling and inference process. Thirdly, the research papers of pathology image analysis based on the MRFs and CRFs are comprehensively summarized and some prevalent methods are discussed, which are grouped according to their tasks and categories of images, respectively. Finally, the conclusion and future directions are given in this section. The review shows that pathology image analysis using the MRFs and CRFs is an increasing topic of interest and improve the performance obviously. Besides, they are believed to apply to more extensive research fields for better solutions to problems in the future.

REFERENCES

- [1] U. Grenander, "Tutorials in Pattern Synthesis," *Brown University, Division of Applied Mathematics*, 1983.
- [2] J. P. Monaco and A. Madabhushi, "Class-Specific Weighting for Markov Random Field Estimation: Application to Medical Image Segmentation," *Medical Image Analysis*, vol. 16, no. 8, pp. 1477–1489, 2012.
- [3] J. Besag, "Spatial Interaction and the Statistical Analysis of Lattice Systems," *Journal of the Royal Statistical Society: Series B (Methodological)*, vol. 36, no. 2, pp. 192–225, 1974.
- [4] S.Z.Li, *Markov Random Field Modeling in Computer Vision*. Japan: Spinger, 1995.
- [5] Y. Zhang, M. Brady, and S. Smith, "Segmentation of Brain MR Images through a Hidden Markov Random Field Model and the Expectation-Maximization Algorithm," *IEEE Transactions on Medical Imaging*, vol. 20, no. 1, pp. 45–57, 2001.
- [6] Q. Wang, "GMM-based Hidden Markov Random Field for Color Image and 3D Volume Segmentation," *arXiv preprint arXiv:1212.4527*, 2012.
- [7] S. Wu and X. Weng, "Image Labeling with Markov Random Fields and Conditional Random Fields," *arXiv preprint arXiv:1811.11323*, 2018.
- [8] B. Yu and Z. Fan, "A Comprehensive Review of Conditional Random Fields: Variants, Hybrids and Applications," *Artificial Intelligence Review*, pp. 1–45, 2019.
- [9] A. McCallum, D. Freitag, and F. C. Pereira, "Maximum Entropy Markov Models for Information Extraction and Segmentation," in *ICML*, 2000, pp. 591–598.
- [10] L. Rabiner and B. Juang, "An Introduction to Hidden Markov Models," *IEEE assp magazine*, vol. 3, no. 1, pp. 4–16, 1986.
- [11] J. Lafferty, A. McCallum, and F. C. Pereira, "Conditional random fields: Probabilistic Models for Segmenting and Labeling Sequence Data," 2001.
- [12] X. Zhang, Y. Jiang, H. Peng, K. Tu, and D. Goldwasser, "Semi-Supervised Structured Prediction with Neural CRF Autoencoder," in *Proceedings of the 2017 Conference on Empirical Methods in Natural Language Processing*, 2017, pp. 1701–1711.
- [13] A. F. Wicaksono and S.-H. Myaeng, "Toward advice Mining: Conditional Random Fields for Extracting advice-Revealing Text Units," in *Proceedings of the 22nd ACM International Conference on Information & Knowledge Management*, 2013, pp. 2039–2048.
- [14] L. Zhuowen and K. Wang, "Human Behavior Recognition Based on Fractal Conditional Random Field," in *2013 25th Chinese Control and Decision Conference (CCDC)*, 2013, pp. 1506–1510.
- [15] S. S. Kruthiventi and R. V. Babu, "Crowd Flow Segmentation in Compressed Domain Using CRF," in *2015 IEEE International Conference on Image Processing (ICIP)*, 2015, pp. 3417–3421.
- [16] D. Y. Liliana and C. Basaruddin, "A Review on Conditional Random Fields as a Sequential Classifier in Machine Learning," in *2017 International Conference on Electrical Engineering and Computer Science (ICECOS)*, 2017, pp. 143–148.
- [17] L.-C. Chen, G. Papandreou, I. Kokkinos, K. Murphy, and A. L. Yuille, "Semantic Image Segmentation with Deep Convolutional Nets and Fully Connected CRFs," *arXiv preprint arXiv:1412.7062*, 2014.
- [18] W. H. Organization, *Guide for Establishing a Pathology Laboratory in the Context of Cancer Control*. US: World Health Organization, 2019.

- [19] W. H. Organization *et al.*, *Guide To Cancer Early Diagnosis*. US: World Health Organization, 2017.
- [20] W. H. Organization, "Early cancer diagnosis saves lives, cuts treatment costs," <https://www.who.int/news-room/detail/03-02-2017-early-cancer-diagnosis-saves-lives-cuts-treatment-costs>, 2017.
- [21] —, "Cancer Diagnosis and Treatment," <https://www.who.int/cancer/treatment/en/>, 2020.
- [22] A. Janowczyk and A. Madabhushi, "Deep Learning for Digital Pathology Image Analysis: A Comprehensive Tutorial with Selected Use Cases," *Journal of Pathology Informatics*, vol. 7, no. 1, pp. 29–29, 2016.
- [23] T. J. Fuchs and J. M. Buhmann, "Computational Pathology: Challenges and Promises for Tissue Analysis," *Computerized Medical Imaging and Graphics*, vol. 35, no. 7-8, pp. 515–530, 2011.
- [24] B. Kong, X. Wang, Z. Li, Q. Song, and S. Zhang, "Cancer Metastasis Detection via Spatially Structured Deep Network," in *International Conference on Information Processing in Medical Imaging*, 2017, pp. 236–248.
- [25] S. Doyle, S. Agner, A. Madabhushi, M. Feldman, and J. Tomaszewski, "Automated Grading of Breast Cancer Histopathology Using Spectral Clustering with Textural and architectural Image Features," in *2008 5th IEEE International Symposium on Biomedical Imaging: From Nano to Macro*, 2008, pp. 496–499.
- [26] F. G. Zanjani, S. Zinger *et al.*, "Cancer Detection in Histopathology Whole-Slide Images Using Conditional Random Fields on Deep Embedded Spaces," in *Medical Imaging 2018: Digital Pathology*, 2018, p. 105810I.
- [27] A. Arnab, S. Zheng, S. Jayasumana, B. Romera-Paredes, M. Larsson, A. Kirillov, B. Savchynskyy, C. Rother, F. Kahl, and P. H. Torr, "Conditional Random Fields Meet Deep Neural Networks for Semantic Segmentation: Combining Probabilistic Graphical Models with Deep Learning for Structured Prediction," *IEEE Signal Processing Magazine*, vol. 35, no. 1, pp. 37–52, 2018.
- [28] H. Fu, Y. Xu, S. Lin, D. W. K. Wong, and J. Liu, "Deepvessel: Retinal Vessel Segmentation via Deep Learning and Conditional Random Field," in *International Conference on Medical Image Computing and Computer-assisted Intervention*, 2016, pp. 132–139.
- [29] S. Manivannan, H. Shen, W. Li, R. Annunziata, H. Hamad, R. Wang, and J. Zhang, "Brain Tumor Region Segmentation Using Local Co-Occurrence Features and Conditional Random Fields," *Technique Report*, 2014.
- [30] C. Wang, N. Komodakis, and N. Paragios, "Markov Random Field Modeling, Inference & Learning in Computer Vision & Image Understanding: a Survey," *Computer Vision and Image Understanding*, vol. 117, no. 11, pp. 1610–1627, 2013.
- [31] H. Y. Chang, C. K. Jung, J. I. Woo, S. Lee, J. Cho, S. W. Kim, and T.-Y. Kwak, "Artificial Intelligence in Pathology," *Journal of Pathology and Translational Medicine*, vol. 53, no. 1, p. 1, 2019.
- [32] C. Li, H. Chen, X. Li, N. Xu, Z. Hu, D. Xue, S. Qi, H. Ma, L. Zhang, and H. Sun, "A Review for Cervical Histopathology Image Analysis Using Machine Vision Approaches," *Artificial Intelligence Review*, pp. 1–42, 2020.
- [33] G. Litjens, T. Kooi, B. E. Bejnordi, a. a. Setio, F. Ciompi, M. Ghafoorian, J. a. Van Der Laak, B. Van Ginneken, and C. I. Sánchez, "A Survey on Deep Learning in Medical Image Analysis," *Medical Image Analysis*, vol. 42, pp. 60–88, 2017.
- [34] S. Wang, D. M. Yang, R. Rong, X. Zhan, and G. Xiao, "Pathology Image Analysis Using Segmentation Deep Learning Algorithms," *The American Journal of Pathology*, 2019.
- [35] M. M. Rahaman, C. Li, X. Wu, Y. Yao, Z. Hu, T. Jiang, X. Li, and S. Qi, "A Survey for Cervical Cytopathology Image Analysis Using Deep Learning," *IEEE Access*, vol. 8, pp. 61 687–61 710, 2020.
- [36] L. He, L. R. Long, S. Antani, and G. R. Thoma, "Histology Image Analysis for Carcinoma Detection and Grading," *Computer Methods and Programs in Biomedicine*, vol. 107, no. 3, pp. 538–556, 2012.
- [37] F. Xing and L. Yang, "Robust Nucleus/Cell Detection and Segmentation in Digital Pathology and Microscopy Images: A Comprehensive Review," *IEEE Reviews in Biomedical Engineering*, vol. 9, pp. 234–263, 2016.
- [38] H. Irshad, A. Veillard, L. Roux, and D. Racoceanu, "Methods for Nuclei Detection, Segmentation, and Classification in Digital Histopathology: A Review Current Status and Future Potential," *IEEE Reviews in Biomedical Engineering*, vol. 7, pp. 97–114, 2013.
- [39] L. He, L. R. Long, S. Antani, and G. Thoma, "Computer assisted Diagnosis in Histopathology," *Sequence and Genome Analysis: Methods and Applications*, vol. 3, pp. 271–287, 2010.
- [40] D. Komura and S. Ishikawa, "Machine Learning Methods for Histopathological Image Analysis," *Computational and Structural Biotechnology Journal*, vol. 16, pp. 34–42, 2018.
- [41] J. Staal, M. D. Abramoff, M. Niemeijer, M. a. Viergever, and B. van Ginneken, "Ridge-Based Vessel Segmentation in Color Images of the Retina," *IEEE Transactions on Medical Imaging*, vol. 23, no. 4, pp. 501–509, 2004.
- [42] A. D. Hoover, V. Kouznetsova, and M. Goldbaum, "Locating Blood Vessels in Retinal Images by Piecewise Threshold Probing of a Matched Filter Response," *IEEE Transactions on Medical Imaging*, vol. 19, no. 3, pp. 203–210, 2000.
- [43] C. G. Owen, a. R. Rudnicka, R. Mullen, S. a. Barman, D. Monekosso, P. H. Whincup, J. Ng, and C. Paterson, "Measuring Retinal Vessel Tortuosity in 10-Year-Old Children: Validation of the Computer-Assisted Image Analysis of the Retina (CAIAR) Program," *Investigative Ophthalmology & Visual Science*, vol. 50, no. 5, pp. 2004–2010, 2009.
- [44] J. Odstrcilik, R. Kolar, a. Budai, J. Hornegger, J. Jan, J. Gazarek, T. Kubena, P. Cernosek, O. Svoboda, and E. Angelopoulou, "Retinal Vessel Segmentation by Improved Matched Filtering: Evaluation on a New High-Resolution Fundus Image Database," *IET Image Processing*, vol. 7, no. 4, pp. 373–383, 2013.
- [45] E. J. Carmona, M. Rincón, J. García-Feijóo, and J. M. Martínez-de-la Casa, "Identification of the Optic Nerve Head with Genetic Algorithms," *Artificial Intelligence in Medicine*, vol. 43, no. 3, pp. 243–259, 2008.
- [46] E. Decencire, X. Zhang, G. Cazuguel, B. Lay, B. Cochener, C. Trone, P. Gain, R. Ordonez, P. Massin, A. Erginay, B. Charton, and J.-C. Klein, "Feedback on a Publicly Distributed Database: the Messidor Database," *Image Analysis & Stereology*, vol. 33, no. 3, pp. 231–234, 2014.
- [47] J. Monaco, J. E. Tomaszewski, M. D. Feldman, M. Moradi, P. Mousavi, A. Boag, C. Davidson, P. Abolmaesumi, and A. Madabhushi, "Probabilistic Pairwise Markov Models: Application to Prostate Cancer Detection," in *Medical Imaging 2009: Image Processing*, 2009, p. 725903.
- [48] J. Xu, J. P. Monaco, R. E. Sparks, and A. Madabhushi, "Connecting Markov Random Fields and Active Contour Models: Application to Gland Segmentation and Classification," *Journal of Medical Imaging*, vol. 4, no. 2, p. 021107, 2017.
- [49] X. Wu, V. Kumar, J. R. Quinlan, J. Ghosh, Q. Yang, H. Motoda, G. J. McLachlan, A. Ng, B. Liu, S. Y. Philip *et al.*, "Top 10 Algorithms in Data Mining," *Knowledge and Information Systems*, vol. 14, no. 1, pp. 1–37, 2008.
- [50] T. Mungle, S. Tewary, D. Das, I. arun, B. Basak, S. agarwal, R. ahmed, S. Chatterjee, and C. Chakraborty, "MRF-ANN: a Machine Learning approach for automated Er Scoring of Breast Cancer Immunohistochemical Images," *Journal of microscopy*, vol. 267, no. 2, pp. 117–129, 2017.
- [51] V. Meas-Yedid, S. Tilie, and J.-C. Olivo-Marin, "Color Image Segmentation Based on Markov Random Field Clustering for Histological Image Analysis," in *Object recognition supported by user Interaction for service robots*, 2002, pp. 796–799.
- [52] C. S. Won, J. Y. Nam, and Y. Choe, "Segmenting Cell Images: a Deterministic Relaxation approach," in *Computer Vision and Mathematical Methods in Medical and Biomedical Image Analysis*. Springer, 2004, pp. 281–291.
- [53] G. Zou, J. Sun, and Y. Ao, "Fuzzy Clustering Method based on Particle Swarm Optimization Used in Pathology Image Segmentation," *Computer Engineering and Design*, vol. 030, no. 22, pp. 5155–5157, 2009.
- [54] A. N. Basavanahally, S. Ganesan, S. Agner, J. P. Monaco, M. D. Feldman, J. E. Tomaszewski, G. Bhanot, and A. Madabhushi, "Computerized Image-Based Detection and Grading of Lymphocytic infiltration in Her2+ Breast Cancer Histopathology," *IEEE Transactions on Biomedical Engineering*, vol. 57, no. 3, pp. 642–653, 2009.
- [55] J. Bioucas-Dias, F. Condeixa, and J. Kovačević, "Alternating Direction Optimization for Image Segmentation Using Hidden Markov Measure Field Models," in *Image Processing: Algorithms and Systems XII*, 2014, p. 90190P.
- [56] A. Salazar-Gonzalez, D. Kaba, Y. Li, and X. Liu, "Segmentation of the Blood Vessels and Optic Disk in Retinal Images," *IEEE Journal of Biomedical Health Informatics*, vol. 18, no. 6, pp. 1874–1886, 2014.
- [57] "Study on Algorithm for Malanoma Recognition based on Dermoscopy, author=Liu, Zhijie," Ph.D. dissertation, University of Electronic Science and Technology of China, 2015.
- [58] M. Paramanandam, M. OByrne, B. Ghosh, J. J. Mammen, M. t. Manipadam, R. Thamburaj, and V. Pakrashi, "Automated Segmentation

- of Nuclei in Breast Cancer Histopathology Images,” *PloS one*, vol. 11, no. 9, p. e0162053, 2016.
- [59] R. Ganjee, R. Azmi, and M. E. Moghadam, “A Novel Microaneurysms Detection Method Based on Local Applying of Markov Random Field,” *Journal of Medical Systems*, vol. 40, no. 3, p. 74, 2016.
- [60] L. Zhao, K. Li, M. Wang, J. Yin, E. Zhu, C. Wu, S. Wang, and C. Zhu, “Automatic Cytoplasm and Nuclei Segmentation for Color Cervical Smear Image Using an Efficient Gap-search MRF,” *Computers in Biology and Medicine*, vol. 71, pp. 46–56, 2016.
- [61] A. GençTav, S. Aksoy, and S. ÖNder, “Unsupervised Segmentation and Classification of Cervical Cell Images,” *Pattern Recognition*, vol. 45, no. 12, pp. 4151–4168, 2012.
- [62] M. Dholey, M. Maity, A. Sarkar, A. Giri, A. Sadhu, K. Chaudhury, S. Das, and J. Chatterjee, “Combining GMM-Based Hidden Markov Random Field and Bag-of-Words Trained Classifier for Lung Cancer Detection Using Pap-Stained Microscopic Images,” in *Advanced Computational and Communication Paradigms*, 2018, pp. 695–705.
- [63] J. Su and S. Liu, “Cell Segmentation Method based on Hidden Markov Random Field,” *Journal of Harbin Engineering University*, pp. 400–405, 2019.
- [64] J. Monaco, J. Tomaszewski, M. Feldman, M. Moradi, P. Mousavi, A. Boag, C. Davidson, P. Abolmaesumi, and A. Madabhushi, “Detection of Prostate Cancer from Whole-Mount Histology Images Using Markov Random Fields,” in *Workshop on Microscopic Image Analysis with Applications in Biology (in conjunction with MICCAI)*, 2008.
- [65] J. Monaco, S. Viswanath, and A. Madabhushi, “Weighted Iterated Conditional Modes for Random Fields: Application to Prostate Cancer Detection,” *Program Committee John Ashburner (University College London) Sylvain Bouix (Harvard Medical School) Tim Cootes (University of Manchester)*, vol. 209, 2009.
- [66] J. P. Monaco, J. E. Tomaszewski, M. D. Feldman, I. Hagemann, M. Moradi, P. Mousavi, A. Boag, C. Davidson, P. Abolmaesumi, and A. Madabhushi, “High-Throughput Detection of Prostate Cancer in Histological Sections Using Probabilistic Pairwise Markov Models,” *Medical Image Analysis*, vol. 14, no. 4, pp. 617–629, 2010.
- [67] J. P. Monaco and A. Madabhushi, “Weighted Maximum Posterior Marginals for Random Fields Using an Ensemble of Conditional Densities from Multiple Markov Chain Monte Carlo Simulations,” *IEEE Transactions on Medical Imaging*, vol. 30, no. 7, pp. 1353–1364, 2011.
- [68] E. Yu, J. P. Monaco, J. Tomaszewski, N. Shih, M. Feldman, and A. Madabhushi, “Detection of Prostate Cancer on Histopathology Using Color Fractals and Probabilistic Pairwise Markov Models,” in *2011 Annual International Conference of the IEEE Engineering in Medicine and Biology Society*, 2011, pp. 3427–3430.
- [69] J. Xu, J. P. Monaco, and A. Madabhushi, “Markov Random Field Driven Region-Based Active Contour Model (MARACEL): Application To Medical Image Segmentation,” in *International Conference on Medical Image Computing and Computer-Assisted Intervention*, 2010, pp. 197–204.
- [70] J. Xu, J. P. Monaco, R. Sparks, and A. Madabhushi, “Connecting Markov Random Fields and Active Contour Models: Application to Gland Segmentation and Classification,” *Journal of Medical Imaging*, vol. 4, no. 2, p. 021107, 2017.
- [71] O. S. Al-Kadi, “Texture Measures Combination for Improved Meningioma Classification Of Histopathological Images,” *Pattern recognition*, vol. 43, no. 6, pp. 2043–2053, 2010.
- [72] C. Sun, C. Li, J. Zhang, F. Kulwa, and X. Li, “Hierarchical Conditional Random Field Model for Multi-Object Segmentation in Gastric Histopathology Images,” *Electronics Letters*, vol. 56, pp. 750–753, 04 2020.
- [73] E. Letters, “Gastric Segmenting,” *Electronics Letters*, vol. 56, no. 15, p. 747, 2020.
- [74] C. Sun, C. L. (corresponding author), J. Zhang, M. M. Rahaman, S. Ai, H. Chen, F. Kulwa, Y. Li, X. Li, and T. Jiang, “Gastric Histopathology Image Segmentation Using a Hierarchical Conditional Random Field,” *Biocybernetics and Biomedical Engineering*, p. Accepted for publication, 2020.
- [75] S. Rachel and A. Madabhushi, “Explicit Shape Descriptors: Novel Morphologic Features for Histopathology Classification,” *Medical Image Analysis*, vol. 17, no. 8, pp. 997–1009, 2013.
- [76] W. H. Organization, “An Introduction to Colposcopy: Indications for Colposcopy, instrumentation, Principles and Documentation of Results,” <https://screening.iarc.fr/colpochap.php?lang=1&chap=4>.
- [77] X. Wu and S. K. Shah, “A Conditional Random Field Model for Cell Segmentation Using Multispectral Data,” in *Workshop on Optical Tissue Image Analysis in Microscopy, Histopathology and Endoscopy (in conjunction with MICCAI)*, 2009.
- [78] J. C. Rajapakse and S. Liu, “Staging Tissues with Conditional Random Fields,” in *2011 Annual International Conference of the IEEE Engineering in Medicine and Biology Society*, 2011, pp. 5128–5131.
- [79] H. Fu, G. Qiu, M. Ilyas, and J. Shu, “GlandVision: A Novel Polar Space Random Field Model for Glandular Biological Structure Detection,” in *British Machine Vision Conference*, 2012, pp. 1–12.
- [80] H. Fu, G. Qiu, J. Shu, and M. Ilyas, “A Novel Polar Space Random Field Model for the Detection of Glandular Structures,” *IEEE Transactions on Medical Imaging*, vol. 33, no. 3, pp. 764–776, 2014.
- [81] R. Farjam, H. Soltanian-Zadeh, K. Jafari-Khouzani, and R. A. Zoroofi, “An Image Analysis approach for automatic Malignancy Determination of Prostate Pathological Images,” *Cytometry Part B: Clinical Cytometry*, vol. 72B, no. 4, pp. 227–240, 2007.
- [82] L. Ladick, C. Russell, P. Kohli, and P. H. S. Torr, “Associative Hierarchical CRFs for Object Class Image Segmentation,” in *2009 IEEE 12th International Conference on Computer Vision*, 2009, pp. 739–746.
- [83] J. Wang, J. D. MacKenzie, R. Ramachandran, and D. Z. Chen, “A Deep Learning approach for Semantic Segmentation in Histology Tissue Images,” in *International Conference on Medical Image Computing and Computer-Assisted Intervention*, 2016, pp. 176–184.
- [84] B. Wu, “Mitosis Detection in Breast Cancer Based on Convolutional Neural Network,” Ph.D. dissertation, Harbin Institute of Technology, 2017.
- [85] F. He, “Research of Key Technologies for Microcell Image Sequence Morphology Analysis,” Ph.D. dissertation, Southeast University, 2017.
- [86] Y. Li and W. Ping, “Cancer Metastasis Detection with Neural Conditional Random Field,” *Computing Research Repository (CoRR)*, vol. abs/1806.07064, 2018.
- [87] Q. Liang, Y. Nan, G. Coppola, K. Zou, W. Sun, D. Zhang, Y. Wang, and G. Yu, “Weakly Supervised Biomedical Image Segmentation by Reiterative Learning,” *IEEE Journal of biomedical and health informatics*, vol. 23, no. 3, pp. 1205–1214, 2018.
- [88] Q. Liang, Y. Nan, S. Xiang, I. Mei, W. Sun, and G. Yu, “Feasibility of Deep Learning Image-Based Segmentation Algorithm in Pathological Section of Gastric Cancer.”
- [89] H. Qu, P. Wu, Q. Huang, J. Yi, G. M. Riedlinger, S. De, and D. N. Metaxas, “Weakly Supervised Deep Nuclei Segmentation Using Points Annotation in Histopathology Images,” in *International Conference on Medical Imaging with Deep Learning*, 2019, pp. 390–400.
- [90] S. B. Jamal, “Use of Spatial Information via Markov and Conditional Random Fields in Histopathological Images,” *IEEE TSP2019*, 2019.
- [91] Z.-P. Konstantinos, F. Henrik, R. SEA, R. Ioannis, J. Yann, and Y. Yinyin, “Superpixel-based Conditional Random Fields (SuperCRF): Incorporating Global and Local Context for Enhanced Deep Learning in Melanoma Histopathology,” *Frontiers in Oncology*, 2019.
- [92] Y. Li, M. Huang, Y. Zhang, J. Chen, H. Xu, G. Wang, and W. Feng, “Automated Gleason Grading and Gleason Pattern Region Segmentation based on Deep Learning for Pathological Images of Prostate Cancer,” *IEEE Access*, vol. 8, pp. 117714–117725, 2020.
- [93] Y. Qiu, J. Cai, X. Qin, and J. Zhang, “Inferring Skin Lesion Segmentation with Fully Connected CRFs based on Multiple Deep Convolutional Neural Networks,” *IEEE Access*, vol. 8, pp. 144246–144258, 2020.
- [94] N. C. Codella, D. Gutman, M. E. Celebi, B. Helba, M. A. Marchetti, S. W. Dusza, A. Kalloo, K. Liopyris, N. Mishra, H. Kittler *et al.*, “Skin Lesion Analysis toward Melanoma Detection: A Challenge at the 2017 International Symposium on Biomedical Imaging (ISBI), Hosted by the International Skin Imaging Collaboration (ISIC),” in *2018 IEEE 15th International Symposium on Biomedical Imaging (ISBI 2018)*, 2018, pp. 168–172.
- [95] T. Mendonça, P. M. Ferreira, J. S. Marques, Marçal, ré RS, and J. Rozeira, “PH 2-A Dermoscopic Image Database for Research and Benchmarking,” in *2013 35th Annual International Conference of the IEEE Engineering in Medicine and Biology Society (EMBC)*, 2013, pp. 5437–5440.
- [96] A. A. Adegun and S. Viriri, “FCN-Based DenseNet Framework for Automated Detection and Classification of Skin Lesions in Dermoscopy Images,” *IEEE Access*, vol. 8, pp. 150377–150396, 2020.
- [97] S. Y. Park, D. Sargent, R. Wolters, and R. W. Lieberman, “Semantic Image Analysis for Cervical Neoplasia Detection,” in *2010 IEEE Fourth International Conference on Semantic Computing*, 2010, pp. 160–165.
- [98] S. Y. Park, D. Sargent, R. Lieberman, and U. Gustafsson, “Domain-Specific Image Analysis for Cervical Neoplasia Detection based on

- Conditional Random Fields,” *IEEE Transactions on Medical Imaging*, vol. 30, no. 3, pp. 867–878, 2011.
- [99] X. Descombes, F. Plourabou, A. Boustani, C. Fonta, G. LeDuc, R. Serduc, and T. Weitekamp, “Brain Tumor Vascular Network Segmentation from Micro-Tomography,” in *Proceedings - International Symposium on Biomedical Imaging*, 2011, pp. 1113–1116.
- [100] J. I. Orlando and M. Blaschko, “Learning Fully-Connected CRFs for Blood Vessel Segmentation in Retinal Images,” in *International Conference on Medical Image Computing and Computer-Assisted Intervention*, 2014, pp. 634–641.
- [101] J. Orlando, E. Prokofyeva, and M. Blaschko, “A Discriminatively Trained Fully Connected Conditional Random Field Model for Blood Vessel Segmentation in Fundus Images,” *IEEE Transactions on Biomedical Engineering*, vol. 64, pp. 16–27, 03 2016.
- [102] H. Fu, Y. Xu, D. Wong, and J. Liu, “Retinal Vessel Segmentation via Deep Learning Network and Fully-Connected Conditional Random Fields,” in *2016 IEEE 13th International Symposium on Biomedical Imaging (ISBI)*, 04 2016, pp. 698–701.
- [103] U. T. Nguyen, A. Bhuiyan, L. A. Park, and K. Ramamohanarao, “An Effective Retinal Blood Vessel Segmentation Method Using Multi-Scale Line Detection,” *Pattern Recognition*, vol. 46, no. 3, pp. 703–715, 2013.
- [104] L. Zhou, Q. Yu, X. Xu, Y. Gu, and J. Yang, “Improving Dense Conditional Random Field for Retinal Vessel Segmentation by Discriminative Feature Learning and Thin-vessel Enhancement,” *Computer methods and Programs in Biomedicine*, vol. 148, pp. 13–25, 2017.
- [105] C. Playout, R. Duval, and F. Chériet, “A Multitask Learning architecture for Simultaneous Segmentation of Bright and Red Lesions in Fundus Images,” in *International Conference on Medical Image Computing and Computer-Assisted Intervention*, 2018, pp. 101–108.
- [106] W. Huang, D. Wen, M. Dewan, Y. Yan, and K. Wang, “Automatic Detection of Optic Disc in Retina Image Using CNN and CRF,” in *2018 IEEE SmartWorld, Ubiquitous Intelligence & Computing, Advanced & Trusted Computing, Scalable Computing & Communications, Cloud & Big Data Computing, Internet of People and Smart City Innovation (SmartWorld/SCALCOM/UIC/ATC/CBDCOM/IOP/SCI)*, 2018, pp. 1917–1922.
- [107] W. Huang, “Research on Detection Methods of Related Targets in Color Fundus Retina Image,” Ph.D. dissertation, Jilin University, 2018.
- [108] B. J. Bhatkalkar, D. R. Reddy, S. Prabhu, and S. V. Bhandary, “Improving the Performance of Convolutional Neural Network for the Segmentation of Optic Disc in Fundus Images Using Attention Gates and Conditional Random Fields,” *IEEE Access*, vol. 8, pp. 29 299–29 310, 2020.
- [109] S. Z. Li, *Markov Random Field Modeling in Image Analysis*. Springer Science & Business Media, 2009.
- [110] A. P. Dempster, N. M. Laird, and D. B. Rubin, “Maximum Likelihood from Incomplete Data via the EM Algorithm,” *Journal of the Royal Statistical Society: Series B (Methodological)*, vol. 39, no. 1, pp. 1–22, 1977.
- [111] P. Krähenbühl and V. Koltun, “Efficient Inference in Fully Connected CRFs with Gaussian Edge Potentials,” in *Advances in Neural Information Processing Systems*, 2011, pp. 109–117.
- [112] S. Zheng, S. Jayasumana, B. Romera-Paredes, V. Vineet, Z. Su, D. Du, C. Huang, and P. H. Torr, “Conditional Random Fields as Recurrent Neural Networks,” in *Proceedings of the IEEE International Conference on Computer Vision*, 2015, pp. 1529–1537.
- [113] Y. LeCun, “Whats Wrong with Deep Learning,” in *IEEE Conference on Computer Vision and Pattern Recognition*, 2015.
- [114] A. S. Iquebal and S. Bukkapatnam, “Unsupervised Image Segmentation via Maximum a Posteriori Estimation of Continuous Max-Flow,” <https://deepai.org/publication/unsupervised-image-segmentation-via-maximum-a-posteriori-estimation-of-continuous-max-flow>, 2018.
- [115] L. M. Koch, M. Rajchl, W. Bai, C. F. Baumgartner, T. Tong, J. Passerat-Palmbach, P. Aljabar, and D. Rueckert, “Multi-Atlas Segmentation Using Partially Annotated Data: Methods and Annotation Strategies,” *IEEE Transactions on Pattern Analysis and Machine Intelligence*, vol. 40, no. 7, pp. 1683–1696, 2017.
- [116] C. Wei, X. Jiang, Z. Tang, W. Qian, and N. Fan, “Context-Based Global Multi-Class Semantic Image Segmentation by Wireless Multimedia Sensor Networks,” *Artificial Intelligence Review*, vol. 43, no. 4, pp. 579–591, 2015.
- [117] R. Meier, U. Knecht, A. Jungo, R. Wiest, and M. Reyes, “Perturb-and-MPM: Quantifying Segmentation Uncertainty in Dense Multi-Label CRFs,” *Computing Research Repository (CoRR)*, 2017.
- [118] A. Zeggada, S. Benbraïka, F. Melgani, and Z. Mokhtari, “Multilabel Conditional Random Field Classification for UAV Images,” *IEEE Geoscience and Remote Sensing Letters*, vol. 15, no. 3, pp. 399–403, 2018.
- [119] C. Mercan, S. Aksoy, E. Mercan, L. G. Shapiro, D. L. Weaver, and J. G. Elmore, “Multi-Instance Multi-Label Learning for Multi-Class Classification of Whole Slide Breast Histopathology Images,” *IEEE Transactions on Medical Imaging*, vol. 37, no. 1, pp. 316–325, 2017.
- [120] P. Zhang, M. Li, Y. Wu, and H. Li, “Hierarchical Conditional Random Fields Model for Semisupervised SAR Image Segmentation,” *IEEE Transactions on Geoscience and Remote Sensing*, vol. 53, no. 9, pp. 4933–4951, 2015.
- [121] S. Kumar and M. Hebert, “A Hierarchical Field Framework for Unified Context-Based Classification,” in *Tenth IEEE International Conference on Computer Vision (ICCV’05) Volume 1*, 2005, pp. 1284–1291.
- [122] Y. Yang, A. Stein, V. A. Tolpekin, and Y. Zhang, “High-Resolution Remote Sensing Image Classification Using Associative Hierarchical CRF considering Segmentation Quality,” *IEEE Geoscience and Remote Sensing Letters*, vol. 15, no. 5, pp. 754–758, 2018.
- [123] M. S. Jain and T. F. Massoud, “Predicting Tumour Mutational Burden from Histopathological Images Using Multiscale Deep Learning,” *Nature Machine Intelligence*, vol. 2, no. 6, pp. 356–362, 2020.
- [124] Z. Ning, X. Zhang, C. Tu, Q. Feng, and Y. Zhang, “Multiscale Context-Cascaded Ensemble Framework (MSC2EF): Application to Breast Histopathological Image,” *IEEE Access*, vol. 7, pp. 150 910–150 923, 2019.
- [125] M. Wang, Z. Dong, Y. Cheng, and D. Li, “Optimal Segmentation of High-Resolution Remote Sensing Image by Combining Superpixels with the Minimum Spanning Tree,” *IEEE Transactions on Geoscience and Remote Sensing*, vol. 56, no. 1, pp. 228–238, 2017.
- [126] Troya-Galvis,rés, P. Gançarski, and L. Berti-Equille, “Remote Sensing Image Analysis by Aggregation of Segmentation-Classification Collaborative Agents,” *Pattern Recognition*, vol. 73, pp. 259–274, 2018.
- [127] J. Takasugi, H. Yamagami, T. Noguchi, Y. Morita, T. Tanaka, Y. Okuno, S. Yasuda, K. Toyoda, Y. Gon, K. Todo *et al.*, “Detection of Left Ventricular Thrombus by Cardiac Magnetic Resonance in Embolic Stroke of Undetermined Source,” *Stroke*, vol. 48, no. 9, pp. 2434–2440, 2017.
- [128] K. López-Linares, N. Aranjuelo, L. Kabongo, G. Maclair, N. Lete, M. Ceresa, A. García-Familiar, I. Macía, and M. a. G. Ballester, “Fully Automatic Detection and Segmentation of Abdominal Aortic Thrombus in Post-Operative CTA Images Using Deep Convolutional Neural Networks,” *Medical Image Analysis*, vol. 46, pp. 202–214, 2018.
- [129] T. Messay, R. C. Hardie, and S. K. Rogers, “A New Computationally Efficient CAD System for Pulmonary Nodule Detection in CT imagery,” *Medical Image Analysis*, vol. 14, no. 3, pp. 390–406, 2010.
- [130] K. Loupos, A. D. Doulamis, C. Stentoumis, E. Protopapadakis, K. Makantasis, N. D. Doulamis, A. Amditis, P. Chrobocinski, J. Victores, R. Montero *et al.*, “Autonomous Robotic System for Tunnel Structural Inspection and Assessment,” *International Journal of Intelligent Robotics and Applications*, vol. 2, no. 1, pp. 43–66, 2018.
- [131] H. Huang, Q. Li, and D. Zhang, “Deep Learning based Image Recognition for Crack and Leakage Defects of Metro Shield Tunnel,” *Tunnelling and Underground Space Technology*, vol. 77, pp. 166–176, 2018.